On the origin of radial anisotropy near subducted slabs in the mid-mantle

William Sturgeon[1], Ana M.G. Ferreira[2,1], Manuele Faccenda[3], Sung-Joon Chang[4]and Lewis Schardong[1,5]

[1]Department of Earth Sciences, Faculty of Mathematical & Physical Sciences, University College London, London, UK

[2]CERIS, Instituto Superior Técnico, Universidade de Lisboa, Lisbon, Portugal

[3]Dipartimento di Geoscienze, Università di Padova, 35131 Padova, Italy

[4]Division of Geology and Geophysics, Kangwon National University, Chuncheon, South Korea

[5]Department of Geophysics and Planetary Sciences, Tel Aviv University, Tel Aviv, Israel

Key Points:

- Geodynamical modeling of anisotropy around slabs shows $V_{SV} > V_{SH}$ in the transition zone and $V_{SH} > V_{SV}$ in the topmost lower mantle.
- Shape-preferred orientation calculations do not fit seismic observations well, notably for deeply penetrating slabs.
- Four possible easy slip systems of bridgmanite are found, agreeing with recent laboratory experiments.

Corresponding author: William Sturgeon, `william.sturgeon.12@ucl.ac.uk`

Abstract

Recent seismic studies indicate the presence of seismic anisotropy near subducted slabs in the transition zone and uppermost lower mantle (mid-mantle). In this study we investigate the origin of radial anisotropy in the mid-mantle using 3-D geodynamic subduction models combined with mantle fabric simulations. These calculations are compared with seismic tomography images to constrain the range of possible causes of the observed anisotropy. We consider three subduction scenarios: (i) slab stagnation at the bottom of the transition zone; (ii) slab trapped in the uppermost lower mantle; and, (iii) slab penetration into the deep lower mantle. For each scenario we consider a range of parameters, including several slip systems of bridgmanite and its grain boundary mobility. Modelling of lattice preferred orientation (LPO) shows that the upper transition zone is characterised by fast-SV radial anisotropy anomalies up to -1.5%. For the stagnating and trapped slab scenarios, the uppermost lower mantle is characterised by two fast-SH radial anisotropy anomalies of $\sim$+2% beneath the slab's tip and hinge. On the other hand, the penetrating slab is associated with fast-SH radial anisotropy anomalies of up to $\sim$+1.3% down to a depth of 2,000 km. Four possible easy slip systems of bridgmanite lead to a good consistency between the mantle modelling and the seismic tomography images: [100](010), [010](100), [001](100) and <110>{$\bar{1}$10}. The anisotropy anomalies obtained from shape-preferred orientation calculations do not fit seismic tomography images in the mid-mantle as well as LPO calculations, especially for slabs penetrating into the deep lower mantle.

Plain Language Summary

Seismology studies reveal that subducting slabs show different characteristics across the Earth; some flatten in the upper mantle (at 660 km depth), others are trapped in the uppermost lower mantle (660-1,200 km depth) and a few penetrate into the deep lower mantle. Subducting slabs cause the surrounding mantle to deform, but the way in which the minerals deform in the mid-mantle (410-1,200 km depth) remains poorly understood.

Geodynamic modelling can help us to infer how the mantle flows and deforms around subduction zones. However, the pattern and evolution of mantle flow around the full range of subduction scenarios has yet to be studied in such detail. Therefore, in this study geodynamic modelling is used to explore a range of mid-mantle parameters that best fit observations around subduction zones from seismology studies. Deformation in the mid-

mantle induced by subducting slabs, including deeply penetrating slabs, is found to be consistent with a mechanism known as dislocation creep, which involves the movement of defects in the crystal lattice of rocks in the deep Earth, and agrees with recent seismic, geodynamic and laboratory studies.

1 Introduction

Subduction zones across the world provide a unique setting for studying mantle deformation and its associated anisotropy. As tectonic plates plunge into the mantle, they drive mantle flow around the subducted slabs. Some slabs penetrate to the lower mantle, whereas others stagnate at the bottom of the transition zone, near the 660 km seismic discontinuity (e.g., Fukao & Obayashi, 2013; Goes et al., 2017). This leads to distinct trajectories of mantle convection, which control the thermo-chemical evolution of our planet (e.g., P. S. Hall et al., 2012). One of the most direct ways to constrain mantle flow is by measuring seismic anisotropy, which can be caused by: (i) lattice-preferred orientation (LPO) of intrinsically anisotropic mantle minerals due to mantle flow; or, (ii) strain-induced shape preferred orientation (SPO) of isotropic materials with highly contrasting seismic properties (for a review see e.g., Chang et al., 2014).

Seismic anisotropy is commonly found in layers of the Earth where deformation and strain are highest (Montagner, 1998). There is abundant evidence of anisotropy in the upper mantle (e.g., Silver, 1996; Fischer & Wiens, 1996) and in the D" region in the lowermost mantle (e.g., Mitchell & Helmberger, 1973; Lay & Helmberger, 1983; Vinnik et al., 1989; Ritsema, 2000; Nowacki et al., 2011). However, in the mid-mantle (∼410-1,200 km), which in this study is considered to be composed of the upper transition zone (UTZ, 410-520 km), lower transition zone (LTZ, 520-660 km) and uppermost lower mantle (ULM, ∼660-1,200 km), the presence of anisotropy is debated (e.g., Beghein & Trampert, 2004; Panning et al., 2010; Chang et al., 2014; De Wit & Trampert, 2015). Both experimental and numerical modelling results suggest that certain mid-mantle minerals are intrinsically anisotropic. In the UTZ, wadsleyite is anisotropic, with a single crystal V_S anisotropy of 18% at ambient conditions, decreasing to ∼9% at pressures corresponding to a depth of 410 km (J. S. Zhang et al., 2018). Tommasi et al. (2004) reported that wadsleyite is able to generate LPO in response to a given flow process and Kawazoe et al. (2013) experimentally found that [001](010) is the dominant slip system of wadsleyite for a water content of 50-230 wt. ppm H_2O. However, Ohuchi et al. (2014) suggested that wad-

sleyite has several slip systems of similar strength for different water content regimes, and each regime will form an LPO. In the LTZ, ringwoodite has been reported to be nearly perfectly isotropic at LTZ pressures (Mainprice et al., 2000). Bridgmanite, constituting 78% of the lower mantle, is anisotropic (e.g., Meade et al., 1995; Wenk et al., 2004; Mainprice et al., 2008; Tsujino et al., 2016). It has been reported that bridgmanite has a single-crystal V_S anisotropy of 33% at ambient conditions (Yeganeh-Haeri, 1994), but that it decreases to 8% at 1,000 km depth when using the extrapolated temperature and pressure derivatives of Wentzcovitch et al. (2004). Such estimates of bridgmanite single-crystal V_S anisotropy have been shown to be even larger when considering elastic properties calculated by Z. Zhang et al. (2013) (Ferreira et al., 2019). Ferropericlase, constituting 16% of the lower mantle, remains nearly isotropic at 660 km depth, but its single-crystal V_S anisotropy increases considerably with pressure, becoming up to 40% in the D" region (Marquardt et al., 2009). It has been shown recently by Muir and Brodholt (2018) that, in contrast to previous views, water does not have a significant effect on lower mantle rheology. However, water may change the activity of the slip systems of bridgmanite, which may in turn affect the resultant anisotropy (e.g., Jung et al., 2006).

Analysis of transmission electron microscopy on wadsleyite polycrystals deformed in compression and simple shear in multi-anvil apparatus showed dislocations in glide configuration as well as subgrains, indicating the presence of dynamic recrystallisation and suggesting deformation by dislocation creep (Dupas et al., 1994; Sharp et al., 1994; Dupas-Bruzek et al., 1998; Thurel & Cordier, 2003; Thurel et al., 2003). Regarding the lower mantle, several seismic studies suggest that it is on average isotropic, apart from the D" region (e.g., Chang et al., 2014). This led to the view that the dominant deformation mechanism in this region is diffusion creep (Karato et al., 1995). High temperature experiments on fabric developments by Karato et al. (1995) suggested that the absence of anisotropy in the lower mantle is strong evidence for deformation by superplasticity, provided that grain size remains reasonably small (Edington et al., 1976). More recently, numerical simulations of creep by Boioli et al. (2017) suggested that dislocation pure climb creep, which does not produce LPO, dominates in bridgmanite. On the other hand, bridgmanite aggregates deformed during laboratory experiments display a clear LPO at relatively small strains (Tsujino et al., 2016; Miyagi & Wenk, 2016). However, the validity of the extrapolation of laboratory experiments to lower mantle conditions is questionable given the extremely different values of stress and strain rate.

Several shear-wave splitting studies have suggested anisotropy in the mid-mantle (e.g., Vinnik et al., 1998), notably near subducting slabs down to the ULM (e.g., Wookey et al., 2002; Chen & Brudzinski, 2003; Wookey & Kendall, 2004; Foley & Long, 2011; Nowacki et al., 2015; Walpole et al., 2017). Several regional analyses focused e.g., on the Tonga-Kermadec region, with Wookey and Kendall (2004) observing fast-SH shear waves with a delay time of 0.7-2.2 s in the mid-mantle, and Foley and Long (2011) finding a ∼1-3 s delay time attributed to the mid-mantle. However, such studies have difficulty in isolating mid-mantle anisotropy from upper mantle effects and have limited depth resolution and azimuthal coverage, which can restrict their interpretation. It has also been possible to image anisotropy in the mid-mantle through global anisotropy tomography studies since the 1980s (e.g., Nataf et al., 1984; Montagner & Tanimoto, 1991; Panning & Romanowicz, 2004; Yuan & Beghein, 2013, 2014). One of the simplest forms of anisotropy, radial anisotropy, corresponds to transverse isotropy with a vertical axis of symmetry, and no azimuthal dependence (e.g., Bodin et al., 2015). Radial anisotropy describes the difference between horizontally and vertically polarised shear waves, which can potentially distinguish between horizontal and vertical mantle flow.

Over the past decade or so, global radially anisotropic models have been developed using different data sets and modelling schemes (for a review, see e.g., Chang et al., 2014). The inclusion of body-wave travel time data allowed for anisotropy to be resolved in the lower mantle (Panning & Romanowicz, 2006; Kustowski et al., 2008; Panning et al., 2010; Auer et al., 2014; Moulik & Ekström, 2014), even if lowermost mantle anisotropy is difficult to resolve globally (e.g., Kustowski et al., 2008; Chang et al., 2015). In addition, to account for trade-offs between isotropic and anisotropic anomalies and discontinuities, discontinuity perturbations have been included in inversions (e.g., Kustowski et al., 2008; Visser et al., 2008; Moulik & Ekström, 2014). The use of huge data sets and, notably, a large number of surface wave overtone dispersion measurements, has led to an improved agreement between models. Chang et al. (2015) quantitatively compared recent models and found: (i) an improved correlation between SGLOBE-rani (Chang et al., 2015) and *savani* (Auer et al., 2014) of 0.5; this is an encouraging improvement compared to previous studies, which do not show correlations larger than 0.3; (ii) fast-SV radial anisotropy anomalies in the transition zone in SGLOBE-rani near subducted slabs, which also appear in some other models (e.g., *savani* and SEMUCB-WM1 (French & Romanowicz, 2014)); and, (iii) fast-SH radial anisotropy anomalies in the ULM in SGLOBE-rani near

subducted slabs (Ferreira et al., 2019), which also appear in *savani*, and seem consistent with shear-wave splitting analyses. Given this increasing volume of observations, it is timely to investigate the origin of anisotropy in the mid-mantle with geodynamic simulations and mantle fabrics calculations, which is the focus of this study.

The interpretation of radial seismic anisotropy is not straightforward and requires a coordinated effort with other scientific disciplines, such as mineral physics and geodynamics (e.g., Chang et al., 2016; Chang & Ferreira, 2019; Ferreira et al., 2019). For example, LPO calculations depend on temperature, deviatoric stress, dominant creep mechanism, the slip systems of anisotropic minerals, their elastic constants and water content (see e.g., Karato et al., 2008; Mainprice, 2015). Yet, many of these properties are imperfectly known, particularly in the deep mantle. Moreover, other mechanisms such as extrinsic anisotropy through SPO also need to be considered (e.g., Faccenda et al., 2019).

Recent advances in computational modelling have provided new insights into the elastic and rheological properties of the mantle. Anisotropy due to strain-induced LPO has been modelled in the upper mantle (e.g., C. E. Hall et al., 2000; Becker et al., 2012; Faccenda & Capitanio, 2013) and in the deeper mantle; in particular, a number of studies have focused on the lowermost mantle (e.g., McNamara et al., 2002; Wenk et al., 2006; Merkel et al., 2007; Walker et al., 2011). In contrast, few studies have focused on the mid-mantle. Nippress et al. (2004) used 2-D subduction models to show that finite strain produced by the slab tip interaction with the 660 km discontinuity could be responsible for anisotropy observed in the ULM. 3-D petrological-thermo-mechanical flow models of dynamic subduction by Faccenda (2014) explored mid-mantle anisotropy produced by strain-induced LPO, indicating that high deviatoric stresses associated with subduction deform transition zone and lower mantle aggregates by dislocation creep. This approach has been subsequently used to interpret seismic observations of anisotropy in the uppermost lower mantle (Ferreira et al., 2019) as well as anomalies associated with a deep plume-slab interaction (Chang et al., 2016). The investigation of mantle flow and seismic anisotropy near subducted slabs in the mid-mantle is particularly difficult because complex 3-D patterns of mantle convection can develop (e.g., Faccenda & Capitanio, 2013; Faccenda, 2014).

In this study we investigate the origin of mid-mantle (transition zone and ULM) anisotropy using 3-D petrological-thermo-mechanical modelling of subduction dynam-

ics combined with mantle fabrics calculations of mineral aggregates (Faccenda, 2014). This work goes beyond that of Faccenda (2014) and Chang et al. (2016) by incorporating a rheological model, and therefore an effective viscosity, that is consistent with 1-D profiles of viscosity inverted from gravity data, including a mid-mantle viscosity hill in the lower mantle (Rudolph et al., 2015; Mitrovica & Forte, 2004). We also incorporate recent mineral physics results and first principle studies of lower mantle elastic constants. We consider a variety of potential slip systems of bridgmanite, and take into account possible contributions of mantle anisotropy from estimates of grain-scale SPO. Recently, Ferreira et al. (2019) used a similar approach to interpret observations of radial anisotropy in the uppermost lower mantle, but here we examine the whole mid-mantle. Moreover, we consider a greater range of subduction styles and modelling parameters, notably by introducing a slab penetrating deeply into the lower mantle, and by using a variety of possible slip systems. The resulting models are compared with tomographic images around subducted slabs, in order to understand the mechanisms responsible for the observed radial anisotropy.

2 Motivation from global radially anisotropic tomography

As explained in the previous section, despite discrepancies in studies of mid-mantle anisotropy, a number of recent seismic studies suggest the presence of radial anisotropy in the mid-mantle near subducted slabs. In this section we show illustrative examples of radial anisotropy in the global model SGLOBE-rani; for full details of the model and its robustness we refer the reader to the studies of Chang et al. (2015) and Ferreira et al. (2019). We focus on this model since we fully know all the details involved in its construction.

Figure 1 and Figure S1 in the Supporting Information show a selection of isotropic and radially anisotropic cross-sections of seismic structure in SGLOBE-rani near subduction zones. A variety of subduction scenarios are shown: (i) slab stagnation at the bottom of the transition zone (e.g., Honshu, Bonin, Northern Chile); (ii) slab trapped in the ULM (e.g., Kurile, Kermadec, Eastern Java); and, (iii) slab penetration into the deep lower mantle (e.g., Central America, Western Java, possibly Northern Peru). Patterns of radial anisotropy near subducted slabs in the mid-mantle show similar patterns across the various subduction zones: the transition zone is characterised by fast-SV radial anisotropy anomalies of up to $\sim$-3%. In addition, a trend of two fast-SH anomalies

of up to ∼+2% are observed beneath the slab in the ULM, one beneath the steeply dipping portion of the slab and one beneath the slab's tip.

In order to explain the presence of mid-mantle anisotropy around subduction zones, we can reduce the possible number of interpretations by comparing seismic tomography with predictions of geodynamic models. In this study we will compare SGLOBE-rani with calculations of radial anisotropy using 3-D geodynamic subduction models.

3 Methodology

3.1 Geodynamical simulations

We use a series of 3-D petrological-thermo-mechanical models in order to simulate subduction, built upon the methodology from Faccenda (2014) and Ferreira et al. (2019). These models use a 3-D geodynamic framework, I3MG, based upon a mixed Eulerian-Lagrangian finite difference scheme (Gerya, 2009). The model domain is defined by 6,000 × 3,000 × 3,000 km, using 293 × 293 × 69 Eulerian nodes (x, y, z coordinates, respectively; where y is the vertical coordinate).

The initial model set-up (Figure S2) includes a 30 km thick crust overlying a 1 Myr old background mantle and a 80 Myr old oceanic plate. The plate, which is 3260 km long, 90 km thick, 1000 km wide, subducts self-consistently aided by a gently dipping 335 km long slab. A strain-dependent low coefficient of friction of μ=0.02-0.005 at zero deformation and at maximum strain, respectively, is set for the crust; this lubricating layer allows self-consistent subduction of the plate. This is then increased at a depth of 100 km to μ=0.1 to simulate crust eclogitisation, ensuring the crust remains strong down to the transition zone.

We define the thermal structure of the model using a half-space cooling model above 90 km depth, and an adiabatic geotherm of 0.5 K·km^{-1} below. Mantle phase transitions are obtained from density and enthalpy maps taken from PERPLE_X (Connolly, 2005) as a function of pressure and temperature for pyrolite. The Clapeyron slope of the mantle discontinuities can be derived from the density map in Figure S2b.

All the model parameters used in our study are shown in Table S1. In order to limit the number of parameters studied, we focus largely on varying the mantle's viscosity to achieve different subduction simulations. We calculate the effective viscosity for a visco-

plastic material by combining a Druger-Prager yielding criterion and low-T Peierls, high-T dislocation and diffusion creep mechanisms (see Table S2 for the equations used). We simulate three subduction scenarios of: (i) slab stagnation at the bottom of the transition zone; (ii) slab trapped in the ULM; and, (iii) slab penetration into the deep lower mantle.

For our subduction scenarios of a slab stagnation at the bottom of the transition zone and trapped in the ULM, we employ a relatively low viscosity (weak) asthenosphere, a viscosity jump at 660 km depth, and a viscosity hill at around 1,500 km depth, producing a strong mid-mantle (Morra et al., 2010; Marquardt & Miyagi, 2015; Rudolph et al., 2015). Deformation in the upper mantle is accommodated mostly by dislocation creep, whereas it is only active at deviatoric stresses above 10-20 MPa in the lower mantle (Figure S2c). Whilst such values are taken from olivine flow laws, it is generally accepted that this amount of stress is sufficient to activate dislocation creep (e.g., McNamara et al., 2002).

The pre-exponential factors for diffusion and dislocation creep in the upper and lower mantle are the only varying rheological parameters in each of our subduction models. This simulates regional variations in the composition of the mantle (e.g., Ballmer et al., 2017). For the deeply penetrating subduction model, the employed pre-exponential factors for diffusion and dislocation creep result in the absence of the mid-mantle viscosity hill, which would otherwise prevent deep slab penetration.

3.2 Mantle fabric modelling

Following Faccenda (2014) and Ferreira et al. (2019), we calculate the strain-induced lattice-preferred orientation (LPO) of Lagrangian aggregates which are passively advected by means of the Eulerian velocity field obtained by the macro-flow modelling. Throughout the model evolution, the fabric development of each aggregate is calculated using a modified version of the kinematic model D-Rex (Kaminski et al., 2004), which accounts for deformation history, non-steady-state deformation and strain-induced LPO of mid-mantle aggregates (e.g., Faccenda & Capitanio, 2012, 2013; Faccenda, 2014).

We use a harzburgitic upper mantle composition (Ol:Ens=70:30, 0-410 km depth) and a pyrolitic mantle composition in the transition zone (Wd:Grt=60:40, 410-520 km; Rw:Grt=60:40, 520-660 km) and lower mantle (Brd:Fp=80:20, 660-3,000 km) (Mainprice,

2015). Whole crystal aggregates undergo phase transitions at arbitrary density crossovers that represent the boundary between two different rock types (Ol:Ens→Wd:Grt=3,650 kg·m^{-3}; Wd:Grt→Rw:Grt=3,870 kg·m^{-3}; Rw:Grt→Brd:Fp=4,150 kg·m^{-3}) (Figure S2). During subduction, upper mantle and transition zone mantle aggregates are entrained around the slab down into the lower mantle, except near the slab's tip (Figure S3). Given that little is known about the topotactical growth of crystal aggregates undergoing phase transitions given a pre-existing fabric, we adopt the approach of resetting the LPO after each phase transition by randomising the crystal orientation.

We only compute the fabric development for phases that display significant single-crystal visco-elastic anisotropy, such as olivine, enstatite, wadsleyite and bridgmanite, and only for the fraction of viscous deformation accommodated by dislocation creep. Therefore crystal aggregates of cubic phases, including ringwoodite, garnet and ferropericlase, are orientated randomly throughout the model evolution, as they are mostly isotropic in the mid-mantle (e.g., Carrez et al., 2007). In this study, we only display anisotropy generated by significantly deformed aggregates due to the subducting slab (whereby ln $\left(\frac{FSE_{max}}{FSE_{min}}\right)>$ 0.5). This is consistent with our interpretation of anisotropy anomalies near the slabs in the seismic tomography, which have been shown to be statistically distinct groups of anomalies by a cluster analysis (Chang & Ferreira, 2019).

In our models, the ratio of dislocation to diffusion creep is stress-dependent, which is accounted for in the large-scale flow model. A low transition stress value favouring dislocation creep is used for the upper mantle and transition zone (Turcotte & Schubert, 2014), whereas in the lower mantle the dislocation creep mechanism is only active above deviatoric stresses of 10-20 MPa (Figure S2c and Figure 2a-f) (e.g., McNamara et al., 2002).

In order to calculate the strain-induced LPO of anisotropic minerals, we use the normalised Critical Resolved Shear Stress (CRSS) for slip systems of olivine, enstatite and wadsleyite from available experimental data as compiled in Faccenda (2014). For bridgmanite, we test several potential slip systems proposed from experimental studies and from ab-initio simulations (e.g., Cordier et al., 2004; Wenk et al., 2004; Mainprice et al., 2008). At ULM pressures and temperatures we consider: [100](010), [100](001), [010](100), [001](100), [001](010), [001]{$\bar{1}$10}, <$\bar{1}$10>(001), <110>{$\bar{1}$10}. In turn, each slip system was tested by imposing a CRSS five times lower than all other slip systems

(e.g., Tommasi et al., 2004). Whilst this method considers only the softest slip system at a time, it remains a reasonable simplification when dynamic crystallisation is efficient enough. We use bridgmanite elastic tensors and their P-T derivatives derived from Z. Zhang et al. (2013) at ULM conditions (Table S3). We can then obtain the full elastic tensor of each aggregate by Voigt-averaging the crystal elastic properties (scaled at local P-T conditions) according to their volume and orientation. For further comparison, we obtain another fabric from static (0 K) ab-initio atomic scale modelling run at ULM pressures (e.g., Carrez et al., 2007; Mainprice et al., 2008).

We test the effect of the grain boundary mobility (M^*) on the strength and location of the computed anisotropy (Figure 3a-c). In D-Rex, M^* is a dimensionless parameter that controls the efficiency of grain-boundary migration (GBM), a process in which grains with low internal energy grow at the expense of grains with high internal energy (Kaminski & Ribe, 2001). In deformed polycrystalline aggregates, newly formed grains, having undergone recrystallisation, have low internal energy and are well orientated with the easy slip system to accommodate flow. Therefore, they grow more than other grains and dominate the LPO. The higher the M^*, the faster the LPO forms.

There are also other parameters that affect the computed anisotropy, such as the nucleation rate (λ^*) and grain boundary sliding, which can be modelled by the threshold volume fraction below which grains do not deform anymore by dislocation creep (χ) (i.e. do not rotate and have zero internal energy) and the relative CRSS of different slip systems. We use λ^*=5 and confirmed that using λ^*>5 does not lead to a significant variation of LPO strength (Kaminski & Ribe, 2001; Faccenda, 2014). For $\lambda^* < 2$, although the anisotropy is stronger and more dominated by hard grains, the LPO does not agree with that found by (Mainprice et al., 2008) nor with experiments in which there is a clear alignment of one of the crystallographic orientations with the shear direction at very low strain (e.g., Tsujino et al. (2016); see Figures S4 and S5 in the Supporting Information). Regarding grain boundary sliding, we use χ=0.3 (Kaminski et al., 2004). If we increase it, then only the very large grains will deform by dislocation creep, and thus the LPO will be weaker. On the other hand, if we decrease χ even further, we would only slightly strengthen the LPO as the LPO is dominated by the very large grains. χ =0 makes no sense because the dynamic recrystallisation and grain size reduction/growth are intrinsic processes of dislocation creep. Furthermore, reducing the contrast in the CRSS among the different slip systems, decreases the strength of the LPO as more slip systems are

competing to accommodate the strain. Hence, for the sake of simplicity, in this study we choose to test M^* since it has been shown to have the most direct effect on the magnitude of the anisotropy (Kaminski & Ribe, 2001; Boneh et al., 2015). In the upper mantle, olivine has a M^* value of 125±75 taken from model predictions by Kaminski and Ribe (2001) and calibrated against the experimental results from S. Zhang and Karato (1995). In the transition zone, M^* of wadsleyite is set to 125 following the results of Faccenda (2014). For bridgmanite, we vary this constant between 10 (Boneh et al., 2015) and 200 as there is currently little available data to calibrate it. Figure 3a-c shows that increasing M^* in the lower mantle increases the strength of the computed radial anisotropy beneath the slab.As explained in the caption of Figure 3, we only display anisotropy that has been induced by the subducting slab. This is supported by a clustering analysis by Chang and Ferreira (2019), which showed that the anisotropy anomalies around subducted slabs in SGLOBE-rani are a statistically distinct class of anomalies.

In all mantle fabric models used in this study, the M^* value for bridgmanite is set to 125 because it provides a radial anisotropy of ∼+2% beneath the slab. This is consistent with the seismic tomography images in Figure 1 (and Figure S1), and with shear-wave splitting measurements (e.g., Walpole et al., 2017). In addition, bridgmanite's M^* value needs to be high to justify the LPO with the very low amount of deformation induced by the stagnating slab. Lower values of M^* would lead to a poor fit to the observations (Figure 3a-c).

While it is generally accepted that dislocation creep is the dominant deformation mechanism in the upper mantle and transition zone (e.g., Karato & Wu, 1993; Weertman & Weertman, 1975; Kohlstedt & Goetze, 1974; Trampert & van Heijst, 2002; Shimojuku et al., 2009), we explore the effect of the level of deformation absorbed by dislocation creep in bridgmanite on the LPO calculations. In light of recent experiments by Girard et al. (2015), it was reported that bridgmanite crystals are likely to absorb less deformation than the bulk deformation in the lower mantle because they are stiffer than ferropericlase. Thus, we compare the results obtained when bridgmanite absorbs only 30% of the bulk deformation with those obtained when bridgmanite absorbs all deformation. The results, shown in Figure 3, show that when bridgmanite absorbs 30% of the deformation (Figure 3d,e,f), the resultant ULM anisotropy is very weak (∼+0.5%). On the other hand, when bridgmanite absorbs all the deformation (Figure 3a,b,c) the resultant ULM anisotropy is more consistent with that found in the seismic tomogra-

phy images. However, it is worth noting that, even when bridgmanite absorbs only 30% of the deformation, significant ULM anisotropy could be generated with a substantially larger value of M^* or, with a higher amount of subduction-induced deformation than considered in this study or, as mentioned above, with a lower nucleation rate or grain boundary sliding.

In addition to LPO, extrinsic radial anisotropy is also estimated by modelling grain-scale shape-preffered orientation (SPO) using the effective medium theory, following the approach of Backus (1962), Faccenda et al. (2019) and Ferreira et al. (2019) A short summary of the approach used can be found in the Supporting Information (Text S1).

4 Results

In this section we present the results obtained from our 3-D modelling approach for the three subduction scenarios considered. We recall that these different scenarios were achieved mainly by varying the viscosity contrast between the upper and lower mantle, for the simulation parameters presented in the Table S1. The subduction models are compared with tomography images. To aid in their comparison, we interpolate our mantle fabrics calculations into a grid with spacing 200×100×200 km (x, y, z co-ordinates, respectively), which is more comparable with the resolution of the tomography models than the higher resolution used in the geodynamical simulations (∼20×20×40 km). In the future we plan to filter the geodynamical models using the resolution matrix of the tomography models. However, given the global parameterisation used in the tomography models, that is an effort that goes beyond the scope of this study.

4.1 Slab stagnating at the bottom of the transition zone

Figure 4 and Movie S1 show the results obtained for a slab stagnating at the bottom of the transition zone. The slab arrives at the 660 km discontinuity after ∼8 Ma, at a shallow dip angle, owing to a fast trench retreat. The viscosity jump at 660 km depth, together with the negative Clapeyron slope of the 660 km discontinuity and the shallow dip angle, generate relatively low stresses at this depth (Christensen, 1996), ultimately leading to slab stagnation.

Viscosity-depth profiles for each of our subduction models are shown in Figure S6. For the stagnating case (Figure S6b), the effective viscosity of the surrounding mantle

is reduced by the subducting slab compared to the background mantle (with the exception of the sharp peak caused by the high viscosity of the slab itself). This is shown in the upper mantle but is most evident below 660 km depth. Figure 2g shows how the strain rate is high below the hinge of the retreating slab, which decreases the effective viscosity of the lower mantle and reduces the viscosity contrast with the overlying transition zone. In turn, this facilitates the entrainment of mantle transition zone material below 660 km depth.

Sub-horizontal green velocity vectors near the stagnant part of the slab in Figure 2g show that the slab's tip advances slowly over the 660 km discontinuity. This explains the low strain rate below the slab's tip. Strain rate is higher above the stagnating plate because of the return flow opposite to the direction of plate motion. Subduction induces a lower mantle upwelling beyond the slab's tip and up to the right boundary of the model (6,000 km in the x-coordinate, at a relatively low velocity). The induced mantle flow is fastest above the stagnant part of the slab, where the trench retreats. It is worth noting that this leads to some lower mantle regions in Figure S6a with lower viscosity than the upper mantle. This is possible given what we know of the real Earth, based on the history of slab subduction. In particular, a number of slab avalanche events have been documented by van der Meer et al. (2018); these slabs would have greatly loaded the 660 km discontinuity, increasing the stress on the lower mantle and thus reducing its viscosity.

LPO generation can be explained by studying the strain the slab induces on the surrounding mantle. Figure 5 and Movie S2 show the maximum finite strain ellipsoid (FSE) axis on the mantle surrounding the slab. Horizontal sliding of the slab over the 660 km discontinuity generates simple shear deformation in the mid-mantle near the stagnant part of the slab. The maximum FSE axis in the ULM is oriented parallel to the stagnant part of the slab and strain is highest beneath the slab where there is contact with the 660 km discontinuity, and also surrounding the slab's tip. High strain beneath the slab's tip is generated upon contact with the 660 km discontinuity; this produces an area of fast-SH radial anisotropy of $\sim$+2%. Subsequent trench retreat encourages stagnation and the loading of the slab on the 660 km discontinuity generates further strain accommodated by dislocation creep (Figure 2a). Hence, the anisotropy builds away from the slab's tip, forming a second fast-SH radial anisotropy anomaly beneath the steeply dipping portion of the slab, again of $\sim$+2%. The fast-SH anisotropy anomalies are confined

within the 660-1,000 km depth range and show some separation. The UTZ is characterised by ∼-1.5% fast-SV radial anisotropy due to anisotropic wadsleyite. Part of the UTZ above the stagnant part of the slab remains isotropic, due to upwelling and downwelling of the mantle, producing constant phase changes of olivine to wadsleyite and LPO resetting. Fast-SV radial anisotropy anomalies of <-1% are present beyond the slab's tip due to induced poloidal flow rotating the lower mantle aggregates.

In order to further understand the nature of the observed anisotropy anomalies, we ran the fabrics calculations keeping track of the initial rock type for each aggregate (Figure S3). We find an interesting upwelling of transition zone material in the upper mantle wedge. Moreover, Figure S3 shows that except near the slab tip, the region with positive radial anisotropy is made mostly of upper mantle and transition zone aggregates that have been dragged down into the lower mantle (and have transformed into lower mantle aggregates) by the subducting plate. Figure 4a shows good agreement between the radial anisotropy in the seismic tomography images and our LPO fabric calculations for a slab stagnating at the 660 km discontinuity. At least qualitatively, the modelled LPO replicates well the observed anisotropy in the mid-mantle. In the uppermost mantle, the seismic tomography images show negative ξ perturbations which do not appear in the geodynamics models. This is possibly due to (i) the fossil slab anisotropy yielding negative ξ perturbations when the slab is dipping above a certain angle (e.g., Song & Kawakatsu, 2012), while the slab in our modelling is isotropic, and (ii) upwellings triggered by the slab, which are not considered in the geodynamical modelling. The computed ULM anisotropy shows two separate anomalies, with one anomaly beneath the slab's tip and the other beneath the steeply dipping portion of the slab. Nevertheless, these anomalies are less separated than in the seismic tomography images. As explained in the methods section, we tested nine possible slip systems of bridgmanite in the LPO calculations (Figure 4b). Upon comparison with the tomography images, it is clear that four slip systems are compatible with the observed fast-SH radial anisotropy anomalies in the ULM: [100](010), [010](100), [001](100) and $<110>\{\bar{1}10\}$.

As previously reported by Ferreira et al. (2019), modelled grain-scale SPO also replicates well the fast-SH radial anisotropy anomalies observed in the subslab, of up to ∼+2.5% due to the large contrast in mineral isotropic elastic properties in the region between the post-spinel and the post-garnet reactions. However, there is less separation between the two anisotropic anomalies than in the LPO calculations, and they are present down to

greater depths (∼1,100 km) than when considering a LPO mechanism. On the other hand, the SPO modelling is not compatible with the fast-SV radial anisotropy anomalies observed in the transition above the stagnant part of the slab.

4.2 Slab trapped in the uppermost lower mantle

Slab penetration through the 660 km discontinuity is achieved by reducing the viscosity contrast between the upper and lower mantle, as can be seen in Figure S6c-d. In this case, the subduction rate is slower than that of the slab stagnating at the bottom of the transition zone. The slab's tip reaches the 660 km discontinuity after ∼14 Ma, and with a steeper dip angle than in the stagnating case (Movie S3). This generates a large stress on the discontinuity, facilitating penetration over ∼40 Ma.

The creation of radial anisotropy in the ULM is similar to that seen in the stagnating case, as can be seen in Figure 6 and Movie S3. When the slab's tip hits the 660 km discontinuity and consequently begins to stagnate, the large generated stress leads to the first fast-SH radial anisotropy anomaly in the ULM. The slab's tip then remains relatively stationary whilst trench retreat causes the slab to unload across the 660 km discontinuity. This generates further stress at the discontinuity, which leads to the second fast-SH anisotropy anomaly in the ULM. Eventually, the stagnant part of the slab penetrates through the 660 km discontinuity into the ULM. Strain-induced LPO calculations lead to fast-SV anomalies up to ∼-1.5% in the UTZ and to fast-SH anomalies of ∼+1.7% in the ULM.

During penetration through the 660 km discontinuity, the entrained material beneath the slab, which causes the fast-SH radial anisotropy observed, is pushed downwards to a depth extent of ∼1,300 km. The velocity vectors shown in Figure 2h show a downward motion at a relatively fast velocity (red arrows around the slab), resulting in the forcing down of the subslab material. The consequent penetration, after a stable period of stagnation, takes place in ∼7 Ma. During this period, the velocity of the mantle in the whole model domain is also larger than in the stagnating case due to a faster subduction rate, and there is a noticeably larger return flow. The mantle moves fastest in the upper mantle above the slab, but unlike the stagnating case, mantle flow is also fast beneath the slab due to slab penetration.

Strain beneath the penetrating part of the slab is higher than strain beneath the stagnant slab in the previous scenario, but also acts over a larger depth range, as seen in Figure 5b, and in Movie S4. This is due to the lower viscosity of the lower mantle than in the stagnating scenario, and to the slab arriving at the 660 km discontinuity at a steeper angle, generating a larger stress on the discontinuity.

Figure 6b shows the radial anisotropy produced when considering the nine possible bridgmanite slip systems previously stated. We find that four slip systems lead to radial anisotropy compatible with the anisotropy observed in the seismic tomography: [100](010), [010](100), [001](100) and <110>{$\bar{1}$10}. This agrees with those found in the stagnating slab scenario. SPO modelling again shows fast-SH anisotropy below the slab. However, the anisotropy anomalies around the slab in the lower mantle are only up to +1% (peaking at +1.4% beneath the slab's tip) due to the majorite-bridgmanite phase transformation, which is weaker than in the seismic tomography images. Similar to the previous section, SPO modelling also yields fast-SH radial anisotropy in the transition zone, which disagrees with fast-SV radial anisotropy observed in both the seismic tomography and LPO images.

4.3 Slab penetrating deep into the lower mantle

By further decreasing the effective viscosity of the lower mantle compared to the two previous subduction scenarios (see Table S1), the slab penetrates below 1,000 km depth as seen in Figure S6e, Figure 7a, and Movie S5. Slab penetration is helped by a steeper dip angle than in the previous two cases when the slab reaches the 660 km discontinuity, by slow trench retreat and by a weaker resistance imposed by the 660 km discontinuity. Indeed, the slab bends slightly at the 660 km discontinuity due to the viscosity increase, and consequently a large stress is induced around the slab's tip (see Movies S5 and S6). However, the viscosity contrast between the upper and lower mantle is not strong enough to prevent slab penetration and thus, the slab is able to continue penetrating deep into the lower mantle.

Figure 7a shows that fast-SV radial anisotropy anomalies are present in the ULM, whilst fast-SH radial anisotropy anomalies, of up to ∼+1.3% are present beneath the slab's tip. Movie S5 shows how the fast-SH radial anisotropy is created upon slab tip interaction with the 660 km discontinuity and how its strength increases with further subduc-

tion. Strain generated beneath the slab's tip is distributed over a larger area (see Figure 5c,f and Movie S6) than in the two previous sections, thus generating a larger area of induced anisotropy but of weaker strength than in the two previous subduction scenarios. Figure 2i shows that the strain rate is much larger in the entire model domain compared to the previous two subduction scenarios. This is due to a faster rate of subduction, hence a faster and larger poloidal flow is induced in the mantle. Similarly to the trapped slab scenario, flow is vertical all around the end of the slab, producing a fast-SV anisotropy anomaly of ∼-1%. The UTZ yields some fast-SV radial anisotropy anomalies, although the majority of the transition zone remains isotropic due to the large poloidal flow resetting anisotropy at phase change boundaries.

Figure 7b shows that the same four slip systems, as in the two previous sections, lead to seismic anisotropy comparable to the seismic tomography cross-sections. Grain-scale SPO modelling yields a pattern of anisotropy similar to the LPO modelling. The ULM remains largely isotropic, but fast-SH radial anisotropy anomalies appear above and below the slab's tip at depths of ∼1,200-1,800 km. However, the strength of the fast-SH radial anisotropy is significantly weaker than that seen in the LPO model, at ∼+0.3%. This does not match the seismic tomography image shown in Figure 7a.

5 Discussion

Our study presents calculations of radial anisotropy in the mid-mantle for three subduction scenarios. LPO and SPO anisotropy mechanisms have been considered, with LPO leading to anisotropic features more consistent with observations than a SPO mechanism, especially around penetrating slabs. This is highlighted in Figure S7, where radial anisotropy due to SPO is significantly weaker in the deeply penetrating case compared to the LPO. Specifically, no radial anisotropy greater than +1% develops due to SPO in the deeply penetrating slab scenario.

5.1 Transition zone

Figure 8 compares 1-D profiles of depth-dependent radial anisotropy between the three models of subduction and seismic tomography. It is important to note that these profiles are averages of the geodynamic models and of the tomographic images of subduction regions, and therefore radial anisotropy values are smaller than the maximum

values previously stated. The geodynamic models (Figure 8a, b and c) coherently show that the transition zone is characterised by fast-SV radial anisotropy anomalies (ξ<1%) of on average ∼0.5% when considering LPO modelling, but SPO modelling implies the transition zone is isotropic, or has fast-SH radial anisotropy (ξ>1%). Given that the seismic tomography 1-D profiles at subduction regions (Figure 8d) show ∼-0.5% fast-SV anisotropy, LPO can explain this observation but SPO cannot.

Many shear-wave splitting studies struggle to separate contributions of mid-mantle anisotropy from the transition zone and the ULM. However, Nowacki et al. (2015) found shear-wave splitting of ≤2.4 s in the transition zone, attributing this to the presence of hydrous phases in the region but not to the development of LPO, disagreeing with our results. Chen and Brudzinski (2003) found SH waves arriving up to 3 s earlier than SV waves in the transition zone in the Fiji-Tonga region. Whilst this finding is not consistent with the results presented in this study, it does agree with the presence of a plume interacting with the Tonga-Kermadec slab (Chang et al., 2016).

5.2 Uppermost lower mantle

For the uppermost lower mantle, Figures 8a, b and c show that four slip systems of bridgmanite ([100](010), [010](100), [001](100) and <110>{$\bar{1}$10}) yield fast-SH radial anisotropy anomalies. The tomography images for the subduction zone regions plotted in Figure 8d are comparable to the results for the slip systems in Figures 8a, b and c, agreeing with an average maximum fast-SH radial anisotropy value of +0.5% in the ULM, but not below 1,200 km depth. Whilst the seismic tomography suggests that subduction regions have radial anisotropy anomalies of ξ<1% in the lower mantle beneath 1,200 km depth, all three geodynamic models show anomalies that remain ξ>1%. This could be explained by the fact that the resolution of the tomography images is limited beneath ∼1,400 km depth (Chang et al., 2015). On the other hand, this could also suggest that our results are affected by errors in the model parameters, such as grain boundary mobility and relative slip system activities.

When a slab reaches the 660 km seismic discontinuity, it is expected to produce large stresses in the ULM, which in turn can induce mineral alignment, producing anisotropy (e.g., Nippress et al., 2004). Our results confirm this. Indeed, our calculations of LPO lead to a pattern of anisotropy in the ULM similar to that observed in the SGLOBE-

rani and *savani* tomographic models (i.e., two separated fast-SH anomalies of up to +2% beneath stagnant slabs and next to penetrating slabs). The comparison of our LPO modelling to the seismic tomography, to first order, fits the assumption that LPO is randomly re-set at phase changes. The support of this hypothesis, as opposed to inheritance of LPO across phase changes, provides an interesting insight into this relatively unknown area of interest. The inheritance of LPO at phase changes is important to consider in future studies and requires further constraints from laboratory experiments. For slabs stagnating at the bottom of the upper mantle, SPO calculations around the 660 km seismic discontinuity are also compatible with the seismic images.

Several shear-wave splitting studies have reported observations of seismic anisotropy in the ULM broadly compatible with fast-SH radial anisotropy anomalies (e.g., Wookey et al., 2002; Wookey & Kendall, 2004; Mohiuddin et al., 2015). In addition, studies in the Tonga-Kermadec region show that SH waves lead SV by a few seconds (Wookey & Kendall, 2004), which was interpreted as due to either strain-induced LPO or to SPO of subducted material into the ULM. Mohiuddin et al. (2015) observed significant splitting (delay times >1 s) of S phases at the base of the transition zone in subduction regions. They hypothesised a layer of ∼5% anisotropy with a thickness of ∼200 km in the mid-mantle around stagnating slabs. However, they also found that the strength of anisotropy and the thickness of the layer trade off directly; thus, their results are comparable to the values found in this study, since we find weaker anisotropy (∼+2%) in a thicker region (∼540 km). A subsequent shear-wave splitting study by Walpole et al. (2017) reported tilted transverse isotropy in the ULM with a fast symmetry axis orientated sub-parallel to the subduction direction, agreeing with our results. Splitting times of ∼1 s in the ULM, would require a layer of 2% anisotropy ∼180 km thick. Given that the thickness of the anisotropic anomalies in tomographic images is likely affected by limitations in resolution (Chang et al., 2015), this is broadly compatible with our results.

Faccenda (2014) conducted the first calculations of seismic anisotropy around subduction zones and obtained ∼+2% fast-SH radial anisotropy anomalies down to ∼1,000 km depth. However, that study did not test potential slip systems of bridgmanite or take into account possible anisotropy contributions from SPO. Also, although the rheology of the lower mantle is still largely unknown, the mantle viscosity values used in this study are likely more realistic than when using the olivine flow law used in Faccenda (2014).

5.3 Bridgmanite slip systems

The four potential easy slip systems of bridgmanite identified in this study agree with recent uni-axial deformation experiments in a Kawai-type deformation-DIA apparatus (Tsujino et al., 2016) who found a bridgmanite fabric dominated by the slip system [001](100), at ULM conditions of 25 GPa and 1,873 K. Miyagi and Wenk (2016) used a diamond anvil cell apparatus to report bridgmanite's dominant slip system as [100], [010] and <110> on the (001) planes, at pressures <55 GPa, agreeing with our slip directions but not with our slip plane. An earlier study by Cordier et al. (2004) suggested [100](001) and [010](001) dislocations based on X-ray line-broadening analysis of samples recovered from a deformation experiment at 25 GPa and 1,673 K, but both slip systems disagree with our findings.

Slip systems of bridgmanite have also been investigated numerically using the Peierls-Nabarro model and calculation of generalised stacking faults and the Peierls-Nabarro-Galerkin model to evaluate Peierls stresses (Ferré et al., 2007; Gouriet et al., 2014). These studies find that [010](100) and [100](010) should be the easiest slip systems, agreeing with our results. A study of the interaction between the Samoan plume and Tonga-Kermadec slab (Chang et al., 2016) highlighted [100](010), [100](001), $<\bar{1}10>(001)$ and $<110>\{\bar{1}10\}$ as potential bridgmanite easy slip systems. Our study agrees with two of these slip systems, suggesting that the results of Chang et al. (2016) may require higher mid-mantle temperature due to the interaction between the slabs and the plume.

5.4 Geodynamic modelling

Our geodynamic modelling of slab subduction relies on a rheological model where the high-temperature effective viscosity strongly depends on the pre-exponential factor and a depth-dependent activation enthalpy for both diffusion and dislocation creep mechanisms. Previous models, such as those in Faccenda (2014), utilised only the olivine flow law with pressure-dependent activation enthalpy, which produces a very high effective viscosity already at 1,000 km depth. In contrast, the present rheological model is more consistent with existing constraints on the 1-D viscosity profile of the Earth, including a viscosity hill in the mid-lower mantle (e.g., Rudolph et al., 2015), and the relative contribution of dislocation creep mechanism in the lower mantle that is significant only at high stresses (e.g, McNamara et al., 2002; Cordier et al., 2004; Mainprice et al., 2008).

The latter effect is needed to prevent lower mantle fabrics and seismic anisotropy to develop everywhere in the lower mantle around subduction zones, which is not observed in the SGLOBE-rani and *savani* tomographic models. For the stagnating scenario, the negative Clapeyron slope and fast trench migration are essential for slab stagnation across the 660 km discontinuity. A layer of reduced viscosity has been suggested to aid in the stagnation of slabs at the 660 km discontinuity (Mao & Zhong, 2018); we performed this test to find that the low viscosity layer had the effect of absorbing more deformation, resulting in a wider area of diffused anisotropy in the ULM. This hindered the separation of two fast-SH anomalies in the ULM, which are observed in the tomography images.

On the other hand, the steeper dip angle of the slab associated with the relative slower trench migration rates in the trapped and penetrating scenarios, respectively, aid slab penetration through the 660 km discontinuity. This agrees with the results of geodynamical modelling by Agrusta et al. (2017), whereby a viscosity increase in the lower mantle is not by itself enough to control subduction dynamics; trench migration and the Clapeyron slope also play an important role. Nippress et al. (2004) used instantaneous 2-D flow calculations in an early subduction setting to investigate lower mantle anisotropy. Despite the differences between their modelling scheme and ours, it is interesting that when comparing an early stage of our FSE modelling for the penetrating slab scenario (as seen in Movie S6) to theirs, we see that in both models the longest FSE axis align in the same direction.

Our rheological model accounts for a combined dislocation-diffusion creep mechanism, similar to that of Hedjazian et al. (2017). We have varied the criteria used to activate dislocation creep by varying the pre-exponential factors of the diffusion and dislocation creep flow laws. This has allowed us to (1) obtain different subduction scenarios, which is not possible with kinematic models such as those of Hedjazian et al. (2017), and, at the same time, (2) vary the contribution of one creep mechanism relative to the other. Unlike this study, Hedjazian et al. (2017) identified areas deformed by diffusion creep in the upper mantle. In our model, dislocation creep is predominant over diffusion creep in most P-T-stress conditions in the upper mantle and transition zone. As a result, the anisotropy at these depths represents an upper bound estimate. Nevertheless, this assumption is realistic for the anisotropy estimated near the slab where stresses are generally high (about 1 MPa), agreeing with the conclusion of McNamara et al. (2002).

5.5 Limitations

As previously mentioned, a study of Girard et al. (2015) found that bridgmanite is substantially stronger than ferropericlase and largely accommodates strain in the lower mantle. Whilst Girard et al. (2015) suggested that bridgmanite only absorbs 30% of deformation in the lower mantle, when taking such results into account in our modelling, we obtained weak fast-SH radial anisotropy anomalies of <+1% in the ULM which are not compatible with the seismic tomography images. In addition, our results disagree with those found in a recent study by Boioli et al. (2017) that suggests a pure climb deformation mechanism whereby seismic anisotropy due to LPO is not present in the lower mantle. It is worth to note, however, that the experimental crystal aggregates deformed by Girard et al. (2015) contain 30% of ferropericlase. If this is the case, it is unclear which other mechanism could explain the observed radial anisotropy anomalies, as grain-scale SPO, for example, does not produce significant anisotropy for penetrating subducting slabs. This is substantially higher than the 17% volume fraction found in pyrolite, with the consequence that bridgmanite could accommodate more deformation at the expense of the less abundant ferropericlase. Our LPO and SPO modelling have only been compared to one tomography model. Ferreira et al. (2019) showed a good level of agreement between the radial anisotropy patterns in SGLOBE-rani and in its contemporaneous *savani* model near slabs in the mid-mantle. Future comparisons with new anisotropy tomography models will be important to further test the geodynamical models.

On the other hand, our micro- and macro-geodynamic modelling also have their own limitations, which are mainly related to the rheological properties of mantle's minerals. In particular, relative slip system activities and the flow law parameters for mantle aggregates are still uncertain, especially in the lower mantle. For mid-mantle aggregates, we only consider the slip system with the lowest CRSS, however, the conclusions of this study may be different if two or more slip systems have the same CRSS. Given the existing large uncertainties of the CRSS of the different slip systems of bridgmanite, investigating the contributions of two or more slip systems remains an area for future work. Nevertheless, this is a common assumption used when the uncertainties of the CRSS of the different slip systems are significantly high (Tommasi et al., 2004), which is the case e.g. for bridgmanite. The contribution to lower mantle anisotropy from ferropericlase is also not taken into account in this study, which has been reported to be the dominant cause of anisotropy across and below the pressure-induced iron spin tran-

sition (below about 1,200 km depth) (Marquardt et al., 2009). There are also trade-offs involved in the modelling, for example between the grain boundary mobility and the amount of deformation absorbed by a mineral, such as bridgmanite. Future mineral physics efforts in these directions will help us better constrain our geodynamic and mantle fabric calculations.

It is worth noting other potential causes of anisotropy in the mid-mantle. At middle-transition zone conditions, representative dense hydrous magnesium silicate (DHMS) phases B and D remain stable. Superhydrous phase B remains less anisotropic than wadsleyite, but in contrast phase D can be more anisotropic than wadsleyite (Mookherjee & Tsuchiya, 2015). However, these minor phases have a limited thermal stability field, being mostly stable within the slab (e.g., Frost, 1999; Pamato et al., 2015). Thus, they are are unlikely to be responsible for large scale anisotropy. Further calculations of extrinsic anisotropy associated with compositional heterogeneity by Faccenda et al. (2019) suggested modest SPO throughout the mantle, apart from around the 660−km discontinuity, where anisotropy could be possibly related to grain−scale shape−preferred orientation. An alternative mechanism to explain the observations is the alignment of fluid-pockets in the uppermost lower mantle. (e.g., Holtzman & Kendall, 2010). These structures could be generated as a consequence of the entrainment of hydrous TZ material at lower mantle depths by the slab. As lower mantle minerals have very low hydrogen solubility, partial melting of the metasomatized mantle rocks could occur. A small fraction of subhorizontally aligned melt pockets would be then sufficient to explain the positive radial anisotropy below stagnating slabs.

6 Conclusion

Using 3-D petrological-thermo-mechanical modelling, three subduction models were investigated: (i) slab stagnation at the bottom of the transition zone; (ii) slab trapped in the ULM; and, (iii) slab penetration into the deep lower mantle. Mantle fabric calculations were conducted to investigate possible contributions to radial anisotropy in the mid-mantle from LPO and SPO mechanisms. The UTZ develops a disjointed mantle fabric of fast-SV radial anisotropy when considering LPO, where induced poloidal flow resets some anisotropy at phase transitions. The LTZ remains isotropic due to the cubic symmetry and low single crystal anisotropy of ringwoodite and garnet aggregates. SPO modelling shows fast-SH radial anisotropy anomalies in the majority of the transition

zone, which does not match the seismic tomography images. Fast-SH radial anisotropy anomalies of ∼+2% appear in the ULM when considering the LPO mechanism, and grain-scale SPO could also contribute to radial anisotropy at ULM depths, but not below deeply penetrating slabs due to the small contrast in isotropic elastic moduli. These observations agree with seismic tomography images and with results from shear-wave splitting analysis (Wookey & Kendall, 2004; Walpole et al., 2017). We tested nine potential slip systems for bridgmanite, of which four lead to a good consistency between the mantle fabric modelling and the seismic tomographic images: [100](010), [010](100), [001](100) and <110>{$\bar{1}$10}. Recent deformation experiments at ULM conditions imply the dominant slip system of bridgmanite is [001](100) (Tsujino et al., 2016), which was also highlighted by this study.

With global radially anisotropic tomographic models starting to show improved correlation, comparing them with geodynamic modelling is proving a powerful tool to interpret seismic anisotropy. Whilst there are still limitations in the geodynamic modelling, in particular the fact that the rheology of the mantle is still largely unknown, this study gives support to LPO being the preferred mechanism for the observed radial anisotropy in the mid-mantle. Given that subducting slabs likely exert high stress in the surrounding mantle, the observed radial anisotropy anomalies suggest that dislocation creep is active in the mid-mantle.

Acknowledgments

This research was initially supported by the Leverhulme Trust (project F/00 204/AS), followed by support by NERC project NE/K005669/1 and the Korea Meteorological Administration Research and Development Program under grant KMI 2018-09312. W.S. was supported by the Natural Environment Research Council [grant number NE/L002485/1]. A.M.G.F. also thanks discussions supported by COST Action ES1401-TIDES. M.F. was supported by the ERC StG #758299 NEWTON and the Progetto di Ateneo FACCP-TRAT12 granted by the Universita‘ di Padova. Geodynamic simulations were performed on Galileo Computing Cluster, CINECA, Italy, thanks to the computational time assigned to M.F. under the NUMACOP, NUMACOP2 and NUMACOP3 projects. We thank our colleagues John Brodholt, David Dobson and Alex song for fruitful discussions. We are grateful to the editor Maureen Long and two anonymous reviewers for their valuable comments, which helped improve this manuscript. We are also grateful to Carolina Lithgow-

Bertelloni and Lars Stixrude for providing HeFESTo's results and to Zhigang Zhang for providing bridgmanite's full elastic constants from ab-initio calculations. The code for the large scale subduction models (I3MG) was kindly provided by Taras Gerya, and the mantle fabric calculations used a modified version of the code D-REX available at `http://www.ipgp.fr/~kaminski/web_doudoud/DRex.tar.gz`. Once published, the results of the geodynamical simulations will be freely available in NERC's data repository. SGLOBE-rani can be downloaded from the IRIS website at `http://ds.iris.edu/ds/products/emc-sglobe-rani/`.

References

Agrusta, R., Goes, S., & van Hunen, J. (2017). Subducting-slab transition-zone interaction: Stagnation, penetration and mode switches. *Earth and Planetary Science Letters*, *464*, 10–23.

Auer, L., Boschi, L., Becker, T., Nissen-Meyer, T., & Giardini, D. (2014). Savani: A variable resolution whole-mantle model of anisotropic shear velocity variations based on multiple data sets. *Journal of Geophysical Research: Solid Earth*, *119*(4), 3006–3034.

Backus, G. E. (1962). Long-wave elastic anisotropy produced by horizontal layering. *Journal of Geophysical Research*, *67*(11), 4427–4440.

Ballmer, M. D., Houser, C., Hernlund, J. W., Wentzcovitch, R. M., & Hirose, K. (2017). Persistence of strong silica-enriched domains in the Earth's lower mantle. *Nature Geoscience*, *10*(3), 236–240.

Becker, T., Lebedev, S., & Long, M. (2012). On the relationship between azimuthal anisotropy from shear wave splitting and surface wave tomography. *Journal of Geophysical Research: Solid Earth*, *117*(B1).

Beghein, C., & Trampert, J. (2004). Probability density functions for radial anisotropy: implications for the upper 1200 km of the mantle. *Earth and Planetary Science Letters*, *217*(1-2), 151–162.

Bodin, T., Capdeville, Y., Romanowicz, B., & Montagner, J.-P. (2015). Interpreting radial anisotropy in global and regional tomographic models. In *The Earth's Heterogeneous Mantle* (pp. 105–144). Springer.

Boioli, F., Carrez, P., Cordier, P., Devincre, B., Gouriet, K., Hirel, P., ... Ritterbex, S. (2017). Pure climb creep mechanism drives flow in Earth's lower mantle.

Science Advances, *3*(3), e1601958.

Boneh, Y., Morales, L. F., Kaminski, E., & Skemer, P. (2015). Modeling olivine CPO evolution with complex deformation histories: Implications for the interpretation of seismic anisotropy in the mantle. *Geochemistry, Geophysics, Geosystems*, *16*(10), 3436–3455.

Bullen, K. (1950). An Earth model based on a compressibility-pressure hypothesis. *Geophysical Journal International*, *6*(s1), 50–59.

Carrez, P., Ferré, D., & Cordier, P. (2007). Peierls–Nabarro model for dislocations in $MgSiO_3$ post-perovskite calculated at 120 GPa from first principles. *Philosophical Magazine*, *87*(22), 3229–3247.

Chang, S.-J., & Ferreira, A. M. (2019). Inference on water content in the mantle transition zone near subducted slabs from anisotropy tomography. *Geochemistry, Geophysics, Geosystems*, *20*(2), 1189– 1201.

Chang, S.-J., Ferreira, A. M., & Faccenda, M. (2016). Upper- and mid-mantle interaction between the Samoan plume and the Tonga-Kermadec slabs. *Nature communications*, *7*, 10799.

Chang, S.-J., Ferreira, A. M., Ritsema, J., Heijst, H. J., & Woodhouse, J. H. (2015). Joint inversion for global isotropic and radially anisotropic mantle structure including crustal thickness perturbations. *Journal of Geophysical Research: Solid Earth*, *120*(6), 4278–4300.

Chang, S.-J., Ferreira, A. M., Ritsema, J., van Heijst, H. J., & Woodhouse, J. H. (2014). Global radially anisotropic mantle structure from multiple datasets: a review, current challenges, and outlook. *Tectonophysics*, *617*, 1–19.

Chen, W.-P., & Brudzinski, M. R. (2003). Seismic anisotropy in the mantle transition zone beneath Fiji-Tonga. *Geophysical Research Letters*, *30*(13).

Christensen, U. R. (1996). The influence of trench migration on slab penetration into the lower mantle. *Earth and Planetary Science Letters*, *140*(1-4), 27–39.

Clauser, C., & Huenges, E. (1995). Thermal conductivity of rocks and minerals. *Rock physics & phase relations: a handbook of physical constants*, 105–126.

Connolly, J. A. (2005). Computation of phase equilibria by linear programming: a tool for geodynamic modeling and its application to subduction zone decarbonation. *Earth and Planetary Science Letters*, *236*(1), 524–541.

Cordier, P., Ungár, T., Zsoldos, L., & Tichy, G. (2004). Dislocation creep in $MgSiO_3$ perovskite at conditions of the Earth's uppermost lower mantle. *Nature*, *428*(6985), 837–840.

Demouchy, S., Mainprice, D., Tommasi, A., Couvy, H., Barou, F., Frost, D., & Cordier, P. (2011). Forsterite to wadsleyite phase transformation under shear stress and consequences for the Earth's mantle transition zone. *Physics of the Earth and Planetary Interiors*, *184*(1), 91–104.

De Wit, R., & Trampert, J. (2015). Robust constraints on average radial lower mantle anisotropy and consequences for composition and texture. *Earth and Planetary Science Letters*, *429*, 101–109.

Dupas, C., Doukhan, N., Doukhan, J.-C., Green, H. W., & Young, T. E. (1994). Analytical electron microscopy of a synthetic peridotite experimentally deformed in the β olivine stability field. *Journal of Geophysical Research: Solid Earth*, *99*(B8), 15821–15832.

Dupas-Bruzek, C., Sharp, T. G., Rubie, D. C., & Durham, W. B. (1998). Mechanisms of transformation and deformation in $Mg_{1.8}Fe_{0.2}SiO_4$ olivine and wadsleyite under non-hydrostatic stress. *Physics of the Earth and Planetary Interiors*, *108*(1), 33–48.

Dziewonski, A. M., & Anderson, D. L. (1981). Preliminary reference Earth model. *Physics of the Earth and Planetary Interiors*, *25*(4), 297–356.

Edington, J. W., Melton, K., & Cutler, C. (1976). Superplasticity. *Progress in Materials Science*, *21*(1-2), 61–170.

Engdahl, E. R., van der Hilst, R., & Buland, R. (1998). Global teleseismic earthquake relocation with improved travel times and procedures for depth determination. *Bulletin of the Seismological Society of America*, *88*(3), 722–743.

Faccenda, M. (2014). Mid mantle seismic anisotropy around subduction zones. *Physics of the Earth and Planetary Interiors*, *227*, 1–19.

Faccenda, M., & Capitanio, F. (2012). Development of mantle seismic anisotropy during subduction-induced 3-D flow. *Geophysical Research Letters*, *39*(11).

Faccenda, M., & Capitanio, F. (2013). Seismic anisotropy around subduction zones: Insights from three-dimensional modeling of upper mantle deformation and SKS splitting calculations. *Geochemistry, Geophysics, Geosystems*, *14*(1), 243–262.

Faccenda, M., Ferreira, A. M., Tisato, N., Lithgow-Bertelloni, C., Stixrude, L., & Pennacchioni, G. (2019). Extrinsic elastic anisotropy in a compositionally heterogeneous Earth's mantle. *Journal of Geophysical Research: Solid Earth*.

Ferré, D., Carrez, P., & Cordier, P. (2007). First principles determination of dislocations properties of $MgSiO_3$ perovskite at 30GPa based on the Peierls–Nabarro model. *Physics of the Earth and Planetary Interiors*, *163*(1), 283–291.

Ferreira, A., Faccenda, M., Sturgeon, W., Chang, S.-J., & Schardong, L. (2019). Ubiquitous mid-mantle anisotropy around subduction zones. *Nature Geoscience*, *12*, 301–306.

Fischer, K. M., & Wiens, D. A. (1996). The depth distribution of mantle anisotropy beneath the Tonga subduction zone. *Earth and Planetary Science Letters*, *142*(1-2), 253–260.

Foley, B. J., & Long, M. D. (2011). Upper and mid-mantle anisotropy beneath the Tonga slab. *Geophysical Research Letters*, *38*(2).

French, S., & Romanowicz, B. (2014). Whole-mantle radially anisotropic shear velocity structure from spectral-element waveform tomography. *Geophysical Journal International*, *199*(3), 1303–1327.

Frost, D. J. (1999). The stability of dense hydrous magnesium silicates in earth's transition zone and lower mantle. *Mantle petrology: field observations and high pressure experimentation: a tribute to Francis R.(Joe) Boyd*, 283–296.

Fukao, Y., & Obayashi, M. (2013). Subducted slabs stagnant above, penetrating through, and trapped below the 660 km discontinuity. *Journal of Geophysical Research: Solid Earth*, *118*(11), 5920–5938.

Gerya, T. (2009). *Introduction to numerical geodynamic modelling*. Cambridge University Press.

Girard, J., Amulele, G., Farla, R., Mohiuddin, A., & Karato, S.-i. (2015). Shear deformation of bridgmanite and magnesiowüstite aggregates at lower mantle conditions. *Science*, aad3113.

Goes, S., Agrusta, R., van Hunen, J., & Garel, F. (2017). Subduction-transition zone interaction: A review. *Geosphere*, *13*(3), 644–664.

Gouriet, K., Carrez, P., & Cordier, P. (2014). Modelling [1 0 0] and [0 1 0] screw dislocations in $MgSiO_3$ perovskite based on the Peierls–Nabarro–Galerkin model. *Modelling and Simulation in Materials Science and Engineering*, *22*(2),

913 025020.

914 Hall, C. E., Fischer, K. M., Parmentier, E., & Blackman, D. K. (2000). The in-
915 fluence of plate motions on three-dimensional back arc mantle flow and shear
916 wave splitting. *Journal of Geophysical Research: Solid Earth*, *105*(B12),
917 28009–28033.

918 Hall, P. S., Cooper, L. B., & Plank, T. (2012). Thermochemical evolution of the
919 sub-arc mantle due to back-arc spreading. *Journal of Geophysical Research:*
920 *Solid Earth*, *117*(B2).

921 Hedjazian, N., Garel, F., Davies, D. R., & Kaminski, E. (2017). Age-independent
922 seismic anisotropy under oceanic plates explained by strain history in the
923 asthenosphere. *Earth and Planetary Science Letters*, *460*, 135–142.

924 Holtzman, B. K., & Kendall, J.-M. (2010). Organized melt, seismic anisotropy, and
925 plate boundary lubrication. *Geochemistry, Geophysics, Geosystems*, *11*(12).

926 Jung, H., Katayama, I., Jiang, Z., Hiraga, T., & Karato, S.-I. (2006). Effect of
927 water and stress on the lattice-preferred orientation of olivine. *Tectonophysics*,
928 *421*(1-2), 1–22.

929 Kaminski, E., & Ribe, N. (2001). A kinematic model for recrystallization and tex-
930 ture development in olivine polycrystals. *Earth and Planetary Science Letters*,
931 *189*(3), 253–267.

932 Kaminski, E., Ribe, N. M., & Browaeys, J. T. (2004). D-Rex, a program for calcu-
933 lation of seismic anisotropy due to crystal lattice preferred orientation in the
934 convective upper mantle. *Geophysical Journal International*, *158*(2), 744–752.

935 Karato, S.-i. (1998). Seismic anisotropy in the deep mantle, boundary layers and
936 the geometry of mantle convection. *Pure & Applied Geophysics*, *151*(2-4),
937 565.

938 Karato, S.-i., Jung, H., Katayama, I., & Skemer, P. (2008). Geodynamic signifi-
939 cance of seismic anisotropy of the upper mantle: new insights from laboratory
940 studies. *Annual Review of Earth and Planetary Sciences*, *36*, 59–95.

941 Karato, S.-i., & Wu, P. (1993). Rheology of the upper mantle: A synthesis. *Science*,
942 *260*(5109), 771–778.

943 Karato, S.-i., Zhang, S., & Wenk, H.-R. (1995). Superplasticity in Earth's Lower
944 Mantle: Evidence from Seismic Anisotropy. *Science*, *270*, 20.

945 Kawazoe, T., Ohuchi, T., Nishihara, Y., Nishiyama, N., Fujino, K., & Irifune, T.

(2013). Seismic anisotropy in the mantle transition zone induced by shear deformation of wadsleyite. *Physics of the Earth and Planetary Interiors*, *216*, 91–98.

Kohlstedt, D., & Goetze, C. (1974). Low-stress high-temperature creep in olivine single crystals. *Journal of Geophysical Research*, *79*(14), 2045–2051.

Kustowski, B., Ekström, G., & Dziewoński, A. (2008). Anisotropic shear-wave velocity structure of the Earth's mantle: A global model. *Journal of Geophysical Research: Solid Earth*, *113*(B6).

Lay, T. (2015). Deep Earth Structure: Lower Mantle and D".

Lay, T., & Helmberger, D. V. (1983). The shear-wave velocity gradient at the base of the mantle. *Journal of Geophysical Research: Solid Earth*, *88*(B10), 8160–8170.

Mainprice, D. (2010). Seismic anisotropy of the deep Earth from a mineral and rock physics perspective. *Treatise on Geophysics, Volume 2: Mineral Physics*, 437.

Mainprice, D. (2015). Seismic anisotropy of the deep earth from a mineral and rock physics perspective. *Treatise on Geophysics (Second Edition). Elsevier, Oxford*, 487–538.

Mainprice, D., Barruol, G., & Ismail, W. B. (2000). The seismic anisotropy of the Earth's mantle: from single crystal to polycrystal. *Earth's Deep Interior: Mineral physics and tomography from the atomic to the global scale*, 237–264.

Mainprice, D., Tommasi, A., Ferré, D., Carrez, P., & Cordier, P. (2008). Predicted glide systems and crystal preferred orientations of polycrystalline silicate Mg-Perovskite at high pressure: Implications for the seismic anisotropy in the lower mantle. *Earth and Planetary Science Letters*, *271*(1), 135–144.

Mao, W., & Zhong, S. (2018). Slab stagnation due to a reduced viscosity layer beneath the mantle transition zone. *Nature Geoscience*, *11*(11), 876.

Marquardt, H., & Miyagi, L. (2015). Slab stagnation in the shallow lower mantle linked to an increase in mantle viscosity. *Nature Geoscience*, *8*(4), 311–314.

Marquardt, H., Speziale, S., Reichmann, H. J., Frost, D. J., Schilling, F. R., & Garnero, E. J. (2009). Elastic shear anisotropy of ferropericlase in Earth's lower mantle. *Science*, *324*(5924), 224–226.

McNamara, A. K., Van Keken, P. E., & Karato, S.-I. (2002). Development of anisotropic structure in the Earth's lower mantle by solid-state convection.

Nature, *416*(6878), 310–314.

Meade, C., Silver, P. G., & Kaneshima, S. (1995). Laboratory and seismological observations of lower mantle isotropy. *Geophysical Research Letters*, *22*(10), 1293–1296.

Merkel, S., McNamara, A. K., Kubo, A., Speziale, S., Miyagi, L., Meng, Y., ... Wenk, H.-R. (2007). Deformation of (Mg, Fe) SiO_3 post-perovskite and D" anisotropy. *Science*, *316*(5832), 1729–1732.

Mishin, Y. A., Gerya, T. V., Burg, J.-P., & Connolly, J. A. (2008). Dynamics of double subduction: Numerical modeling. *Physics of the Earth and Planetary Interiors*, *171*(1), 280–295.

Mitchell, B. J., & Helmberger, D. V. (1973). Shear velocities at the base of the mantle from observations of S and ScS. *Journal of Geophysical Research*, *78*(26), 6009–6020.

Mitrovica, J., & Forte, A. (2004). A new inference of mantle viscosity based upon joint inversion of convection and glacial isostatic adjustment data. *Earth and Planetary Science Letters*, *225*(1-2), 177–189.

Miyagi, L., & Wenk, H.-R. (2016). Texture development and slip systems in bridgmanite and bridgmanite+ ferropericlase aggregates. *Physics and Chemistry of Minerals*, *43*(8), 597–613.

Mohiuddin, A., Long, M. D., & Lynner, C. (2015). Mid-mantle seismic anisotropy beneath southwestern Pacific subduction systems and implications for mid-mantle deformation. *Physics of the Earth and Planetary Interiors*, *245*, 1–14.

Montagner, J.-P. (1998). Where can seismic anisotropy be detected in the Earth's mantle? In boundary layers... *Pure and Applied Geophysics*, *151*(2-4), 223.

Montagner, J.-P., & Tanimoto, T. (1991). Global upper mantle tomography of seismic velocities and anisotropies. *Journal of Geophysical Research: Solid Earth*, *96*(B12), 20337–20351.

Mookherjee, M., & Tsuchiya, J. (2015). Elasticity of superhydrous phase, B, $Mg_{10}Si_3O_{14}(OH)_4$. *Physics of the Earth and Planetary Interiors*, *238*, 42–50.

Morra, G., Yuen, D., Boschi, L., Chatelain, P., Koumoutsakos, P., & Tackley, P. (2010). The fate of the slabs interacting with a density/viscosity hill in the mid-mantle. *Physics of the Earth and Planetary Interiors*, *180*(3), 271–282.

Moulik, P., & Ekström, G. (2014). An anisotropic shear velocity model of the Earth's mantle using normal modes, body waves, surface waves and long-period waveforms. *Geophysical Journal International*, *199*(3), 1713–1738.

Muir, J. M., & Brodholt, J. P. (2018). Water distribution in the lower mantle: Implications for hydrolytic weakening. *Earth and Planetary Science Letters*, *484*, 363–369.

Nakakuki, T., Tagawa, M., & Iwase, Y. (2010). Dynamical mechanisms controlling formation and avalanche of a stagnant slab. *Physics of the Earth and Planetary Interiors*, *183*(1), 309–320.

Nataf, H.-C., Nakanishi, I., & Anderson, D. L. (1984). Anisotropy and shear-velocity heterogeneities in the upper mantle. *Geophysical Research Letters*, *11*(2), 109–112.

Nippress, S., Kusznir, N., & Kendall, J.-M. (2004). Modeling of lower mantle seismic anisotropy beneath subduction zones. *Geophysical Research Letters*, *31*(19).

Nowacki, A., Kendall, J.-M., Wookey, J., & Pemberton, A. (2015). Mid-mantle anisotropy in subduction zones and deep water transport. *Geochemistry, Geophysics, Geosystems*, *16*(3), 764–784.

Nowacki, A., Wookey, J., & Kendall, J.-M. (2011). New advances in using seismic anisotropy, mineral physics and geodynamics to understand deformation in the lowermost mantle. *Journal of Geodynamics*, *52*(3), 205–228.

Ohuchi, T., Fujino, K., Kawazoe, T., & Irifune, T. (2014). Crystallographic preferred orientation of wadsleyite and ringwoodite: Effects of phase transformation and water on seismic anisotropy in the mantle transition zone. *Earth and Planetary Science Letters*, *397*, 133–144.

Pamato, M. G., Myhill, R., Ballaran, T. B., Frost, D. J., Heidelbach, F., & Miyajima, N. (2015). Lower-mantle water reservoir implied by the extreme stability of a hydrous aluminosilicate. *Nature Geoscience*, *8*(1), 75.

Panning, M., Lekić, V., & Romanowicz, B. (2010). Importance of crustal corrections in the development of a new global model of radial anisotropy. *Journal of Geophysical Research: Solid Earth*, *115*(B12).

Panning, M., & Romanowicz, B. (2004). Inferences on flow at the base of Earth's mantle based on seismic anisotropy. *Science*, *303*(5656), 351–353.

Panning, M., & Romanowicz, B. (2006). A three-dimensional radially anisotropic

model of shear velocity in the whole mantle. *Geophysical Journal International*, *167*(1), 361–379.

Ranalli, G. (1995). *Rheology of the Earth*. Springer Science & Business Media.

Ritsema, J. (2000). Evidence for shear velocity anisotropy in the lowermost mantle beneath the Indian Ocean. *Geophysical Research Letters*, *27*(7), 1041–1044.

Rudolph, M. L., Lekić, V., & Lithgow-Bertelloni, C. (2015). Viscosity jump in Earth's mid-mantle. *Science*, *350*(6266), 1349–1352.

Sharp, T. G., Bussod, G. Y., & Katsura, T. (1994). Microstructures in β-$Mg_{1.8}Fe_{0.2}SiO_4$ experimentally deformed at transition-zone conditions. *Physics of the Earth and Planetary Interiors*, *86*(1-3), 69–83.

Shimojuku, A., Kubo, T., Ohtani, E., Nakamura, T., Okazaki, R., Dohmen, R., & Chakraborty, S. (2009). Si and O diffusion in (Mg, Fe) $2SiO_4$ wadsleyite and ringwoodite and its implications for the rheology of the mantle transition zone. *Earth and Planetary Science Letters*, *1*(284), 103–112.

Silver, P. G. (1996). Seismic anisotropy beneath the continents: probing the depths of geology. *Annual Review of Earth and Planetary Sciences*, *24*(1), 385–432.

Song, T.-R. A., & Kawakatsu, H. (2012). Subduction of oceanic asthenosphere: Evidence from sub-slab seismic anisotropy. *Geophysical Research Letters*, *39*(17).

Stixrude, L., & Lithgow-Bertelloni, C. (2011). Thermodynamics of mantle minerals-II. Phase equilibria. *Geophysical Journal International*, *184*(3), 1180–1213.

Thurel, E., & Cordier, P. (2003). Plastic deformation of wadsleyite: I. High-pressure deformation in compression. *Physics and Chemistry of Minerals*, *30*(5), 256–266.

Thurel, E., Cordier, P., Frost, D., & Karato, S.-I. (2003). Plastic deformation of wadsleyite: II. High-pressure deformation in shear. *Physics and Chemistry of Minerals*, *30*(5), 267–270.

Tommasi, A., Mainprice, D., Cordier, P., Thoraval, C., & Couvy, H. (2004). Strain-induced seismic anisotropy of wadsleyite polycrystals and flow patterns in the mantle transition zone. *Journal of Geophysical Research: Solid Earth*, *109*(B12).

Trampert, J., & van Heijst, H. J. (2002). Global azimuthal anisotropy in the transition zone. *Science*, *296*(5571), 1297–1299.

Tsujino, N., Nishihara, Y., Yamazaki, D., Seto, Y., Higo, Y., & Takahashi, E.

(2016). Mantle dynamics inferred from the crystallographic preferred orientation of bridgmanite. *Nature*, *539*(7627), 81–84.

Turcotte, D., & Schubert, G. (2014). *Geodynamics*. Cambridge University Press.

van der Meer, D. G., van Hinsbergen, D. J., & Spakman, W. (2018). Atlas of the underworld: Slab remnants in the mantle, their sinking history, and a new outlook on lower mantle viscosity. *Tectonophysics*, *723*, 309–448.

Vinnik, L. P., Chevrot, S., & Montagner, J.-P. (1998). Seismic evidence of flow at the base of the upper mantle. *Geophysical Research Letters*, *25*(11), 1995–1998.

Vinnik, L. P., Farra, V., & Romanowicz, B. (1989). Observational evidence for diffracted SV in the shadow of the Earth's core. *Geophysical Research Letters*, *16*(6), 519–522.

Visser, K., Trampert, J., Lebedev, S., & Kennett, B. (2008). Probability of radial anisotropy in the deep mantle. *Earth and Planetary Science Letters*, *270*(3), 241–250.

Walker, A., Forte, A., Wookey, J., Nowacki, A., & Kendall, J.-M. (2011). Elastic anisotropy of D" predicted from global models of mantle flow. *Geochemistry, Geophysics, Geosystems*, *12*(10).

Walpole, J., Wookey, J., Kendall, J.-M., & Masters, T.-G. (2017). Seismic anisotropy and mantle flow below subducting slabs. *Earth and Planetary Science Letters*, *465*, 155–167.

Weertman, J., & Weertman, J. R. (1975). High temperature creep of rock and mantle viscosity. *Annual Review of Earth and Planetary Sciences*, *3*(1), 293–315.

Wenk, H.-R., Lonardeli, I., Pehl, J., Devine, J., Prakapenka, V., Shen, G., & Mao, H.-K. (2004). In situ observation of texture development in olivine, ringwoodite, magnesiowüstite and silicate perovskite at high pressure. *Earth and Planetary Science Letters*, *226*(3), 507–519.

Wenk, H.-R., Speziale, S., McNamara, A., & Garnero, E. (2006). Modeling lower mantle anisotropy development in a subducting slab. *Earth and Planetary Science Letters*, *245*(1), 302–314.

Wentzcovitch, R., Karki, B., Cococcioni, M., & De Gironcoli, S. (2004). Thermoelastic Properties of $MgSiO_3$-Perovskite: Insights on the Nature of the Earth's Lower Mantle. *Physical Review Letters*, *92*(1), 018501.

Wookey, J., & Kendall, J.-M. (2004). Evidence of midmantle anisotropy from shear wave splitting and the influence of shear-coupled P waves. *Journal of Geophysical Research: Solid Earth*, *109*(B7).

Wookey, J., Kendall, J.-M., & Barruol, G. (2002). Mid-mantle deformation inferred from seismic anisotropy. *Nature*, *415*(6873), 777–780.

Yeganeh-Haeri, A. (1994). Synthesis and re-investigation of the elastic properties of single-crystal magnesium silicate perovskite. *Physics of the Earth and Planetary Interiors*, *87*(1), 111–121.

Yuan, K., & Beghein, C. (2013). Seismic anisotropy changes across upper mantle phase transitions. *Earth and Planetary Science Letters*, *374*, 132–144.

Yuan, K., & Beghein, C. (2014). Three-dimensional variations in love and rayleigh wave azimuthal anisotropy for the upper 800 km of the mantle. *Journal of Geophysical Research: Solid Earth*, *119*(4), 3232–3255.

Zha, C.-s., Duffy, T. S., Mao, H.-k., Downs, R. T., Hemley, R. J., & Weidner, D. J. (1997). Single-crystal elasticity of β-mg2sio4 to the pressure of the 410 km seismic discontinuity in the earth's mantle. *Earth and Planetary Science Letters*, *147*(1-4), E9–E15.

Zhang, J. S., Bass, J. D., & Schmandt, B. (2018). The elastic anisotropy change near the 410-km discontinuity: Predictions from single-crystal elasticity measurements of olivine and wadsleyite. *Journal of Geophysical Research: Solid Earth*, *123*(4), 2674–2684.

Zhang, S., & Karato, S.-i. (1995). Lattice preferred orientation in olivine due to shear deformation. *Nature*, *375*, 774–777.

Zhang, Z., Stixrude, L., & Brodholt, J. (2013). Elastic properties of $MgSiO_3$-perovskite under lower mantle conditions and the composition of the deep Earth. *Earth and Planetary Science Letters*, *379*, 1–12.

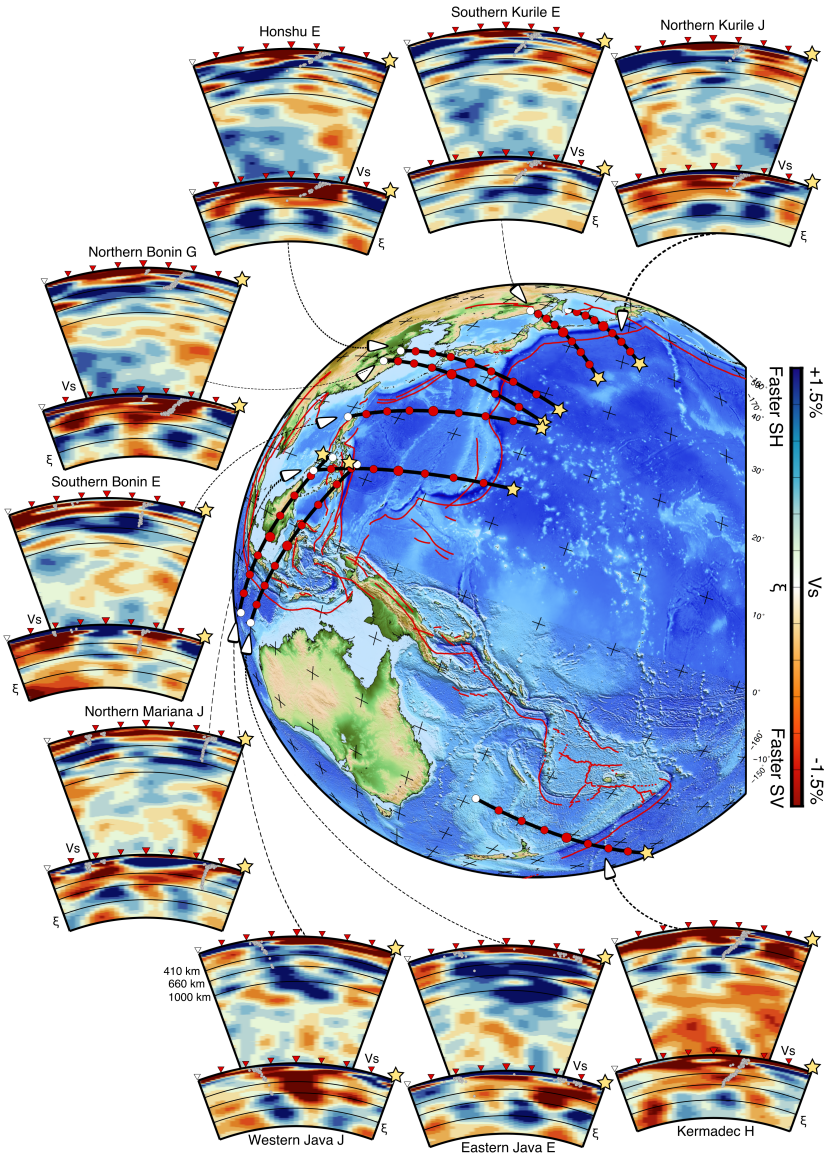

Figure 1. Cross-sections of perturbations in Voigt average and radially anisotropic structure of subduction zones in the Western Pacific. Cross-sections of the global tomography model SGLOBE-rani beneath Northern Kurile, Southern Kurile, Honshu, Northern Bonin, Southern Bonin, Northern Mariana, Western Java, Eastern Java and Kermadec. V_S denotes perturbations in the Voigt average model $\left(V^2_{Voigt}=\frac{2V^2_{SV}+V^2_{SH}}{3}\right)$ with respect to PREM (Dziewonski & Anderson, 1981) down to the core-mantle boundary and ξ denotes perturbations in radial anisotropy $\left(\xi=\frac{V^2_{SH}}{V^2_{SV}}\right)$ down to 1,400 km depth (below this depth the resolution is more limited, see Chang et al., 2015). Focal depths from EHB data (Engdahl et al., 1998) with an upper bound of 60 km are superimposed on the cross-sections as grey circles. The depths of 410 km, 660 km and 1,000 km are represented by solid black lines. For reference, we use the same geographical locations and codes (Cross-sections Northern Kurile J, Southern Kurile E, Honshu E, Northern Bonin G, Southern Bonin E, Northern Mariana J, Western Java J, Eastern Java E and Kermadec H) as in Fukao and Obayashi (2013).

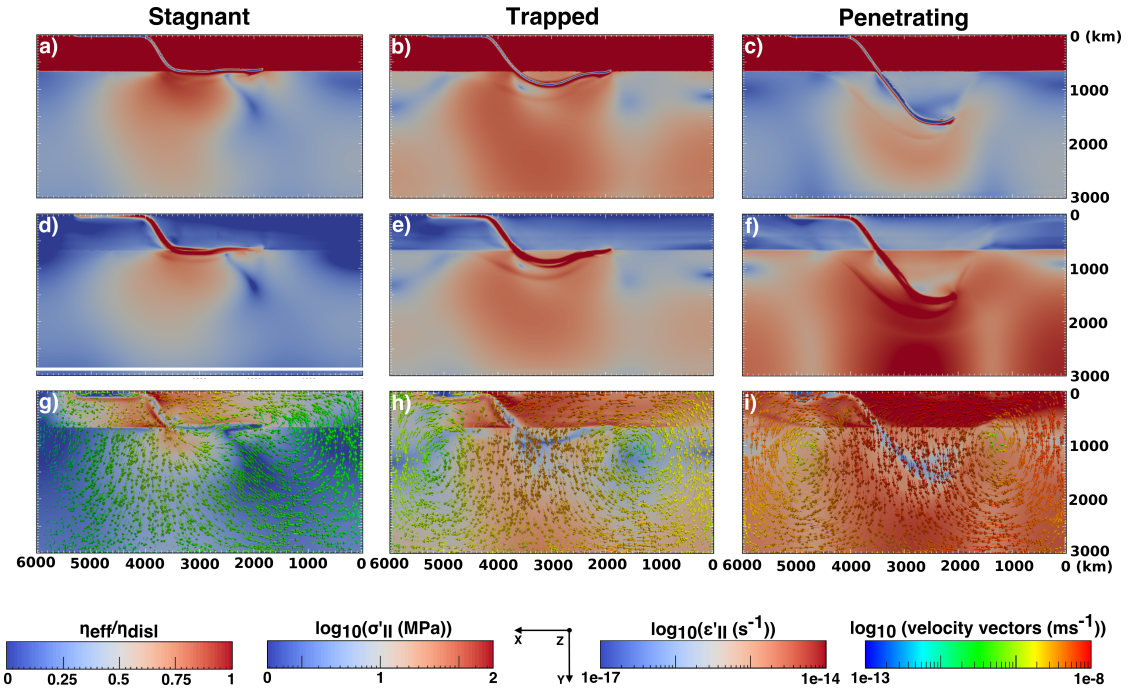

Figure 2. Fraction of deformation accommodated by dislocation creep ($\frac{\eta_{eff}}{\eta_{disl}}$; top row), second invariant of the stress tensor ($\sigma_{II}^{'}$; middle row) and mantle velocity vectors overlain upon the second invariant of the strain tensor ($\varepsilon_{II}^{'}$; bottom row) for stagnant (first column), trapped (second column) and penetrating (third column) slab models.

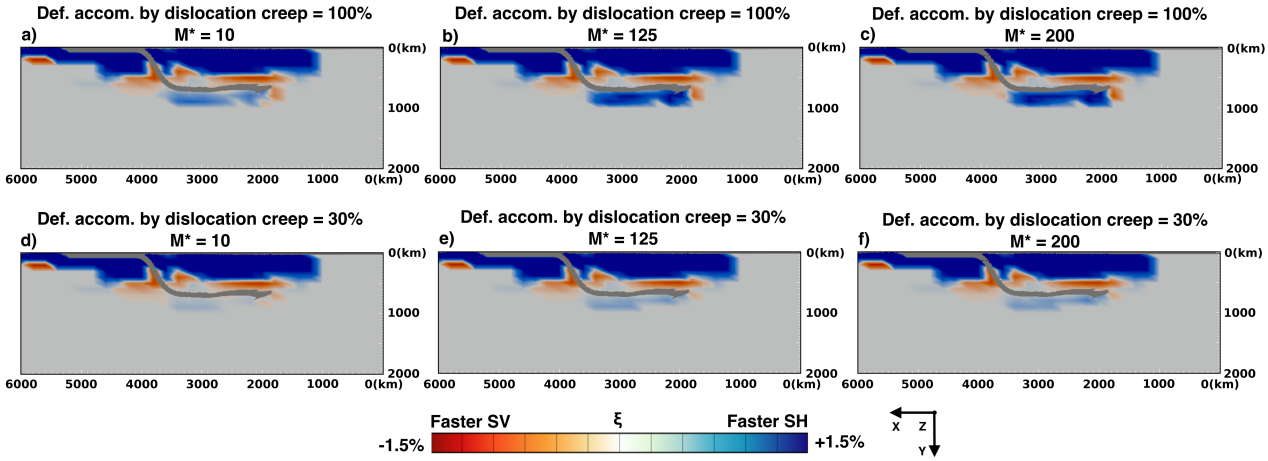

Figure 3. The effects of mantle fabric parameters on radial anisotropy. From left to right: the effect of increasing the grain boundary mobility (M*) to 10 (a, d), 125 (b, e) and 200 (c, f) respectively, where dislocation creep accommodates 100% of the bulk deformation in the lower mantle. From top to bottom: the effect of changing the amount of the bulk deformation accommodated by dislocation creep in the lower mantle from 100% to 30%. All images show radial anisotropy produced by significantly deformed aggregates $\left(\ln\left(\frac{FSE_{max}}{FSE_{min}}\right)>0.5\right)$ and interpolated to a grid with spacings 200 × 100 × 200 km (x, y, z coordinates, respectively). The slab is coloured in grey.

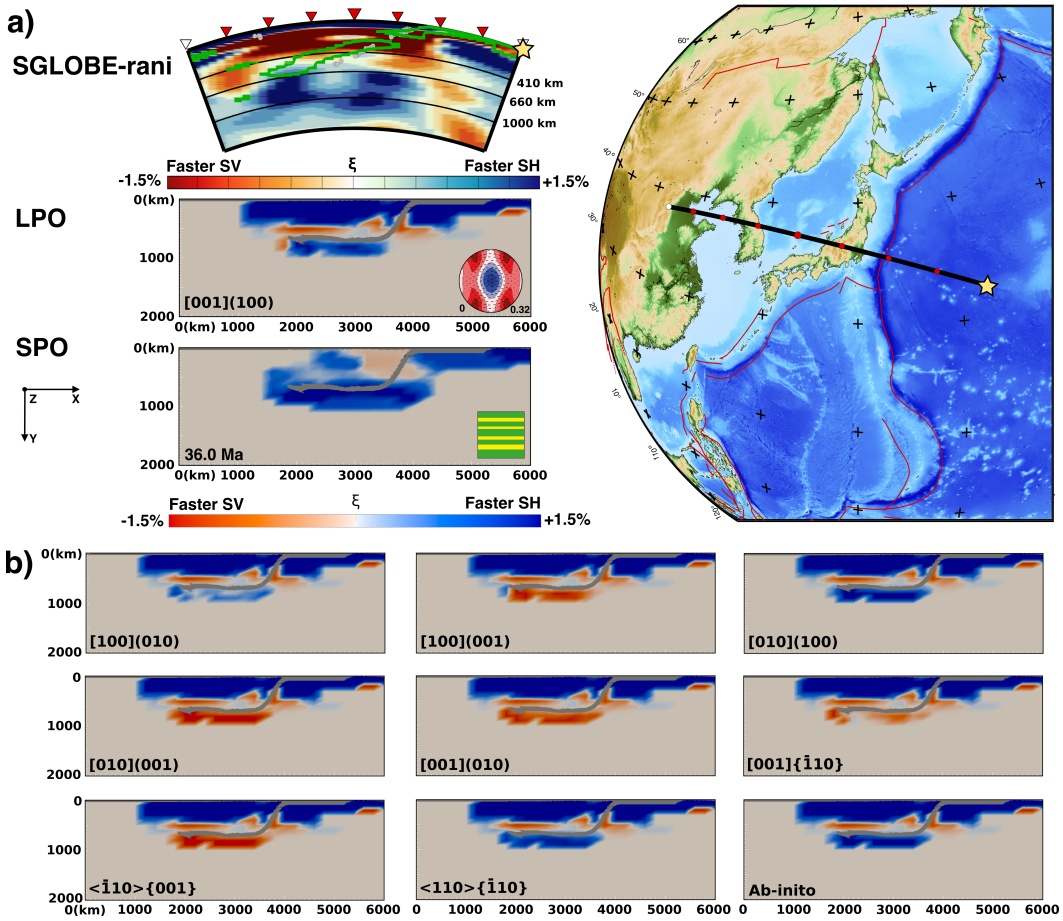

Figure 4. Comparison of seismic tomography with geodynamic modelling for a slab stagnating at the bottom of the transition zone. (a) Comparison between cross-sections of radially anisotropic structure from SGLOBE-rani beneath Honshu and results from geodynamic simulations for a slab stagnating at the bottom of the transition zone. The top image shows a cross-section of perturbations in radial anisotropy $\left(\xi{=}\frac{V_{SH}^2}{V_{SV}^2}\right)$from SGLOBE-rani at Honshu (cross-section Honshu C from Fukao & Obayashi, 2013). The green contours correspond to an outline of the Voigt average fast anomalies from SGLOBE-rani, in the range of 1.25-1.5%. This contour is based on observations and therefore aids in the understanding of the relationship between the slab and anisotropy anomalies. Below this is the computed LPO due to dislocation creep for the [001](100) bridgmanite slip system. We show in the bottom right hand corner the corresponding dV_S (km/s) calculated at lower mantle P-T conditions for a 80:20=Brd:Fp mixture deformed in horizontal simple shear (ξ=1.0); red is minimum; blue is maximum. Cubic MgO crystals are random. The bars in the dV_S maps indicate the polarisation of the fast shear wave component for different propagation directions. Below this is a geodynamic image showing grain-scale SPO assuming a perfectly layered medium for a pyrolitic medium. (b) LPO due to dislocation creep for the nine slip systems of bridgmanite where each slip system is set five times weaker than the rest, ab-initio calculations are from Mainprice et al. (2008). All geodynamic images have a resolution of 200 × 100 × 200 km (x, y, z coordinates, respectively) and show radial anisotropy produced when the minimum ln $\left(\frac{FSE_{max}}{FSE_{min}}\right)$>0.5.

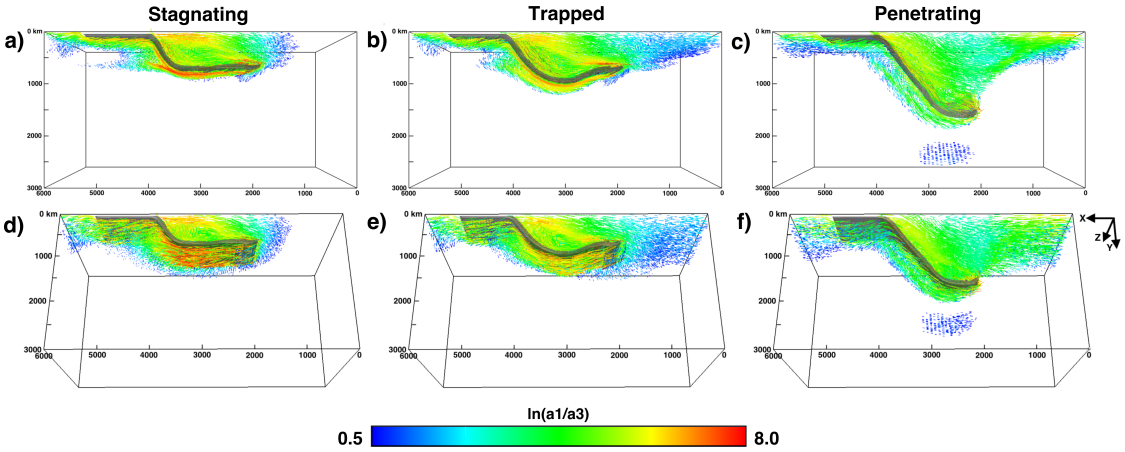

Figure 5. 3-D representations of the finite strain ellipsoid (FSE) for the three subduction scenarios considered in this study. The orientations of the maximum (a_1) FSE axis for the mantle aggregates where $\ln\left(\frac{a_1}{a_3}\right)$>0.5 are shown, providing a clear LPO. The bar length is proportional to $\ln\left(\frac{a_1}{a_3}\right)$, as well as the colour scale. The slab is coloured in grey.

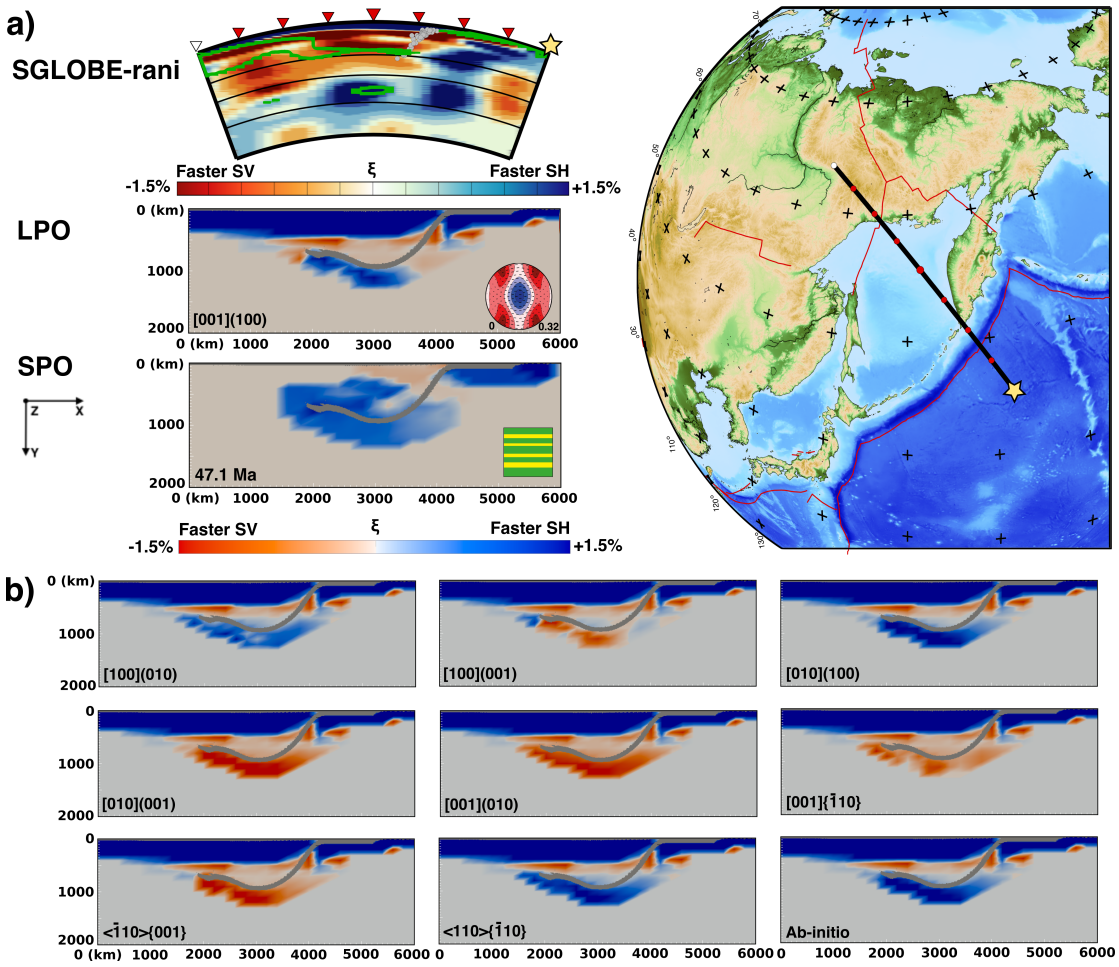

Figure 6. Comparison of the seismic tomography model SGLOBE-rani (Chang et al., 2015) with geodynamic modelling results for a slab trapped in the uppermost lower mantle. Figure details are the same as in Figure 4, but for trapped slab. The seismic tomography image is from Northern Kurile (cross-section Northern Kurile J from Fukao & Obayashi, 2013).

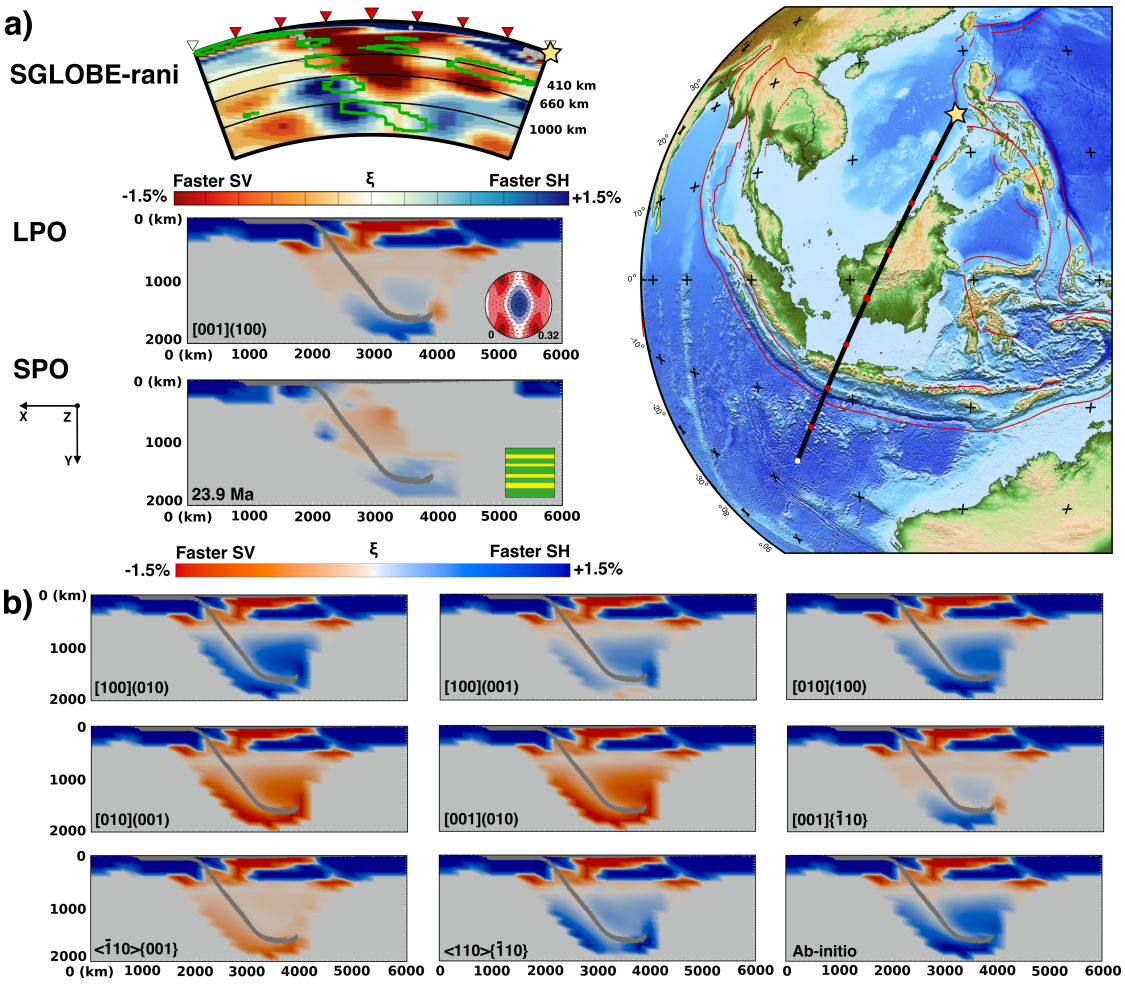

Figure 7. Comparison of the seismic tomography model SGLOBE-rani (Chang et al., 2015) with geodynamic modelling results for slab penetration deep into the lower mantle. Figure details are the same as in Figures 4 and 6, but for a deeply penetrating slab. The seismic tomography image is from Western Java (cross-section Western Java I from Fukao & Obayashi, 2013).

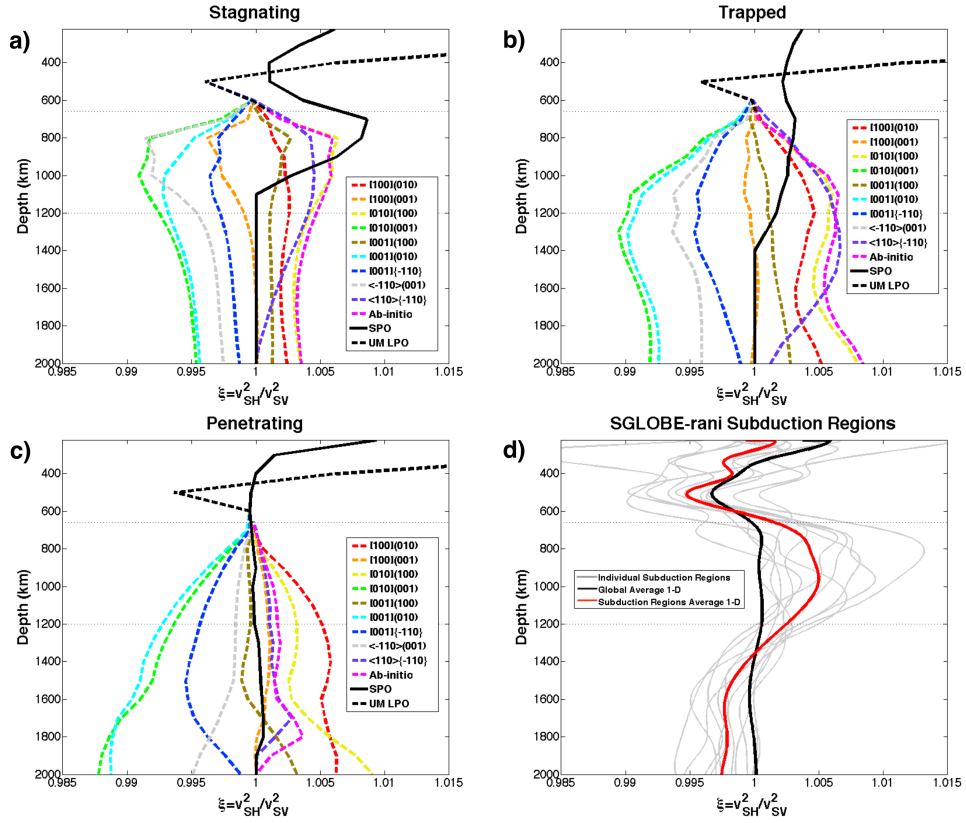

Figure 8. Comparisons of 1-D average radial anisotropy $\left(\xi=\frac{V_{SH}^2}{V_{SV}^2}\right)$ depth profiles from the mantle fabrics simulations (a-c) and from the tomographic model SGLOBE-rani (d) (Chang et al., 2015). The mantle fabric 1-D profiles represent mean values of anisotropy present in the whole model domain as shown in Figures 4, 6 and 7. For LPO, the nine possible bridgmanite slip systems and ab-initio calculations from Mainprice et al. (2008) are plotted, along with SPO calculations. The results are shown for the subduction scenarios of slab stagnation at the bottom of the transition zone (a), slab trapped in the uppermost lower mantle (b) and slab penetration deep into the lower mantle (c). Panel (d) shows depth-dependent 1-D average profiles of radial anisotropy in the model SGLOBE-rani for eleven subduction zones considered: Northern Kurile, Southern Kurile, Honshu, Northern Bonin, Southern Bonin, Northern Mariana, Eastern Java, Western Java, Kermadec, Northern Central America, Northern Peru; their averages are calculated by considering all points in a $2^\circ \times 2^\circ$ grid of the tomographic model SGLOBE-rani that align with all five profiles of each subduction region as defined in Fukao and Obayashi (2013) in grey, their average (red) and the global 1-D average (black). Horizontal dashed lines at 660 km and 1,200 km are used to represent the depth bounds of the uppermost lower mantle. We choose not to interpret anisotropy beneath ~1,400 km in (d) due to the poor balance between SV- and SH-sensitive travel-time data in the body-wave datasets used in current tomography models to constrain lower mantle structure (e.g., Chang et al., 2014, 2015).